

A Computational Fluid Dynamics Investigation of a Novel Ducted Winglet Design.

Richard John Davis, B.Eng.

Submitted to Swansea University in the fulfilment of the requirement for the
Degree of M.Sc. by Research of Aerospace Engineering

Department of Aerospace Engineering
Faculty of Science and Engineering
Swansea University
United Kingdom
2022

Copyright: The Author, Richard J. Davis, 2023.

Keywords

Computational Fluid Dynamics, Wingtip Device, Ducted Winglet, Induced Drag, FLITE3D, Spalart-Allmaras, Drag Reduction.

Abstract

Induced drag is a crucial component of the total drag experienced by aircraft, and reducing it can improve their performance. This study investigates the efficacy of a novel ducted wingtip device in reducing induced drag.

Computational fluid dynamics simulations were performed on an Embraer ERJ145 aircraft with different wingtip configurations, including a ducted winglet, a conventional winglet, and a standard wingtip, across a range of angles of attack. Post-processing techniques such as flow visualization and Trefftz plane analysis were employed to examine the performance of the different wingtip configurations and their induced drag.

Results show that the ducted winglet configuration produced lower values of the coefficient of induced drag across all angles of attack when compared to both the conventional winglet and standard wingtip. However, it also incurred higher form drag penalties due to eddying and separation behaviour identified at the duct. While the ducted winglet produced similar results for the coefficient of total drag at 0 and 1 degree angle of attack compared to both the conventional winglet and standard wingtip, it resulted in higher values at 3, 4, and 5 degrees angle of attack.

Overall, the study suggests that the design of the ducted winglet can reduce induced drag and improve aircraft performance. However, further improvements to the design are necessary to address form drag penalties and enhance its efficacy.

Declarations

This work has not previously been accepted in substance for any degree and is not being concurrently submitted in candidature for any degree.

This thesis is the result of my own investigations, except where otherwise stated. Other sources are acknowledged by footnotes giving explicit references. A bibliography is appended.

I hereby give consent for my thesis, if accepted, to be available for photocopying and for inter-library loan, and for the title and summary to be made available to outside organisations.

The University's ethical procedures have been followed and, where appropriate, that ethical approval has been granted.

Richard John Davis



30th September 2022

Acknowledgements

I would like to thank my primary supervisor Dr Ben Evans for his guidance, support and encouragement throughout my research.

I would like to acknowledge and sincerely thank the friendship, support and counsel offered throughout the project by my fellow researchers Ben Smith, Joseff Parke Sturrock, Jakub Vincalek and Hannah Ditchburn.

I would also like to thank Dan Rödde, Phillip Worth, Kristian McDonald and those at Solis Design for their guidance, patience, trust and support.

Lastly, I would like to thank my family and friends for their endless support and proofreading.

Contents

I	List of Figures	vi
II	List of Tables	vii
III	List of Acronyms and Nomenclature	viii
1	Introduction	1
1.1	Drag	1
1.2	Induced Drag	2
1.3	Drag Reduction	5
1.4	Wingtip Devices	6
1.4.1	Early Development Of Wingtip Devices	7
1.4.2	Development of Winglets	8
1.4.3	Modern Development Of Wingtip Devices	11
1.4.4	The Ducted Winglet	12
1.5	Surface Integration and Far-Field Techniques	13
1.5.1	Surface Integration Techniques	13
1.5.2	Far-Field Techniques	13
1.6	Trefftz Plane	14
2	Hypothesis	15
3	Model Development	16
3.1	Geometry	16
3.2	Flight Conditions	20
3.3	Mesh Generation	21
3.3.1	Mesh Independence Study	22
3.3.2	Final Mesh	24
3.3.3	Inflation Layers	26
3.4	CFD Solver	30
3.4.1	Boundary Conditions	31
3.5	Hardware And Other Software	32
4	Analytical Methodology	33
4.1	Surface Integration	34
4.2	Far-Field Trefftz Plane	35
4.2.1	Software Implementation Of The Trefftz Plane Method	37
4.3	Path Lines	40
4.4	Velocity Planes	41
5	Results	43
5.1	Accuracy and Uncertainty	43
5.2	Surface Integration Coefficient Of Drag Results	45
5.3	Far-Field Coefficient Of Induced Drag Results	46
5.4	Discussion	47
6	Conclusion	49
7	Future Work	50

8	Bibliography	51
9	Appendices	57
9.1	Appendix A	57
9.2	Appendix B	59
9.3	Appendix C	77
9.4	Appendix D	80
9.5	Appendix E	83
9.6	Appendix F	86

I List of Figures

List of Figures

1	Finite wing flow pattern. Fig 5.3 from reference [1]	2
2	Vortex sheet development on a finite wing. Fig 8.1.4 from reference [2]	3
3	Diagram of induced drag Fig 5.6 from reference [1]	4
4	KC-135A Stratotanker flight testing winglets in 1979. Image EC79-11314, Dryden Flight Research Center Photo Collection, NASA[3]	9
5	Two images a and b showing some of the earliest commercial uses of wingtip devices on an Airbus A310-300 and Boeing 747-400 respectively.	10
6	Wingtip devices currently in use or testing stage. Fig 1 from reference [4]	11
7	Figure from a patent for a ducted winglet design. Fig 9 from reference [5]	12
8	Three images, a, b, c, showing the ducted winglet, conventional winglet and standard tip geometries respectively from the leading edge. A fourth image, d, shows the ducted winglet from the wingtip.	16
9	Isometric view of model geometry and far-field fluid domain. . . .	19
10	Mesh independence study results.	23
11	Two images a and b showing zoomed in and zoomed out views respectively of the Embraer ERJ145 geometry with mesh constraints.	25
12	Inflation layers growing from aircraft body into freestream. . . .	28
13	Two images a and b showing the boundary layer flow in the inflation layers and those closest to the surface respectively.	29
14	Boundary conditions on domain.	31
15	Isometric view of Embraer ERJ145 geometry and far-field fluid domain, the Trefftz plane, in blue.	36
16	Mesh on Trefftz plane at $x = 45$ m	37
17	Example MathWorks MATLAB Trefftz Plane analysis output . .	38
18	Example MathWorks MATLAB Trefftz Plane analysis output zoomed in	39
19	DW path lines at angle of attack = 0	40
20	Duct velocity on plane at angle of attack = 0	41
21	Duct velocity vectors on plane at angle of attack = 0	42
22	Example of convergence of C_D	43
23	Example of pattern of performance established in convergence of C_D across all wingtip geometries.	44
24	C_D values for each geometry at each angle of attack	45
25	C_{D_i} values for each geometry at each angle of attack	46

II List of Tables

List of Tables

1	Flight conditions	20
2	Mesh independence study parameters.	22
3	Mesh independence study	23
4	Final mesh properties of sources for cell sizing constraint	24
5	Properties of inflation layers	26
6	Surface Integration FLITE3D C_D results	45
7	Far-field Trefftz plane analysis C_{D_i} results	46

III List of Acronyms and Nomenclature

Acronyms

AIAA American Institute of Aeronautics and Astronautics

CAD Computer Aided Design

CFD Computational Fluid Dynamics

CPU Central Processing Unit

CW Conventional Winglet

DW Ducted Winglet

HPC High Performance Computing

LE Leading Edge

NACA National Advisory Committee for Aeronautics

NASA National Aeronautics and Space Administration

RAM Random Access Memory

RANS Reynolds Averaged Navier-Stokes

Re Reynolds Number

SLUF Steady, Level, Unaccelerated Flight

ST Standard Tip

TE Trailing Edge

VLM Vortex Lattice Method

Nomenclature

α	Angle of Attack
α_i	Induced Angle of Attack
δ	Boundary Layer Thickness
Γ	Circulation Over Wing
\hat{u}	Velocity Perturbations, Downstream Drag Axis Component
\hat{v}	Velocity Perturbations, Lateral Axis Component
\hat{w}	Velocity Perturbations, Lift Axis Component
μ	Dynamic Viscosity
ω	Downwash
ρ	Density
A	Wing Area
b	Span
C_D	Coefficient of Drag
C_{D_i}	Coefficient of Induced Drag
C_{D_o}	Coefficient of Profile Drag
D	Drag
D_i	Induced Drag
E_{max}	Maximum Element Sizing Control
L	Reference Length
r_1	Mesh Control Inner Radius
r_2	Mesh Control Inner Radius
Re	Reynolds Number
S_T	Trefftz Plane
u	Flow Speed
V_∞	Freestream Velocity (Relative Wind)
x/c	Downstream distance from leading edge as fraction of chord length
y	Spanwise Location
y_0	Root Spanwise Location

1 Introduction

1.1 Drag

Drag is described as a “*Retarding force acting upon body in relative motion through fluid, parallel to direction of motion*”[6]. It is defined using the drag equation, equation 1, in which D is drag, C_D is the coefficient of drag, ρ is the freestream fluid density, V_∞ is the freestream velocity, and A is the reference area[1, 7].

$$D = C_D \frac{1}{2} \rho V_\infty^2 A \quad (1)$$

For a finite wing in subsonic flow the coefficient of drag is the sum of the coefficient of profile drag, C_{D_o} , and the coefficient of induced drag, C_{D_i} , as defined by equation 2[1, 7].

$$C_D = C_{D_o} + C_{D_i} \quad (2)$$

The profile drag is dependent on the shape, or profile, of the body. It is the sum of the skin friction drag and the form drag (also often referred to as pressure drag). The induced drag is a consequence of any finite length wing producing lift.

Reducing the induced drag (and as can be seen in equations 1 and 2, the total drag of an aircraft by consequence) is desirable and can result in improved performance including reduced fuel burn and increased maximum range[8].

1.2 Induced Drag

As a wing produces lift, the fluid passing above and below the wing reduces in pressure. However, the fluid above the wing reduces by a larger magnitude and consequently there is a pressure imbalance between the fluid moving across the upper and lower surfaces of the wing.

In the context of a finite length wing, this pressure imbalance resolves at the wingtip, where the higher pressure air below the wing moves towards the lower pressure air above the wing to equalise the pressure imbalance. Due to the presence of the wing, this results in a spanwise velocity component moving outboard in the high pressure air below the wing, and a spanwise velocity component moving inboard in the low pressure air above the wing. This can be seen in Figure 1 below.

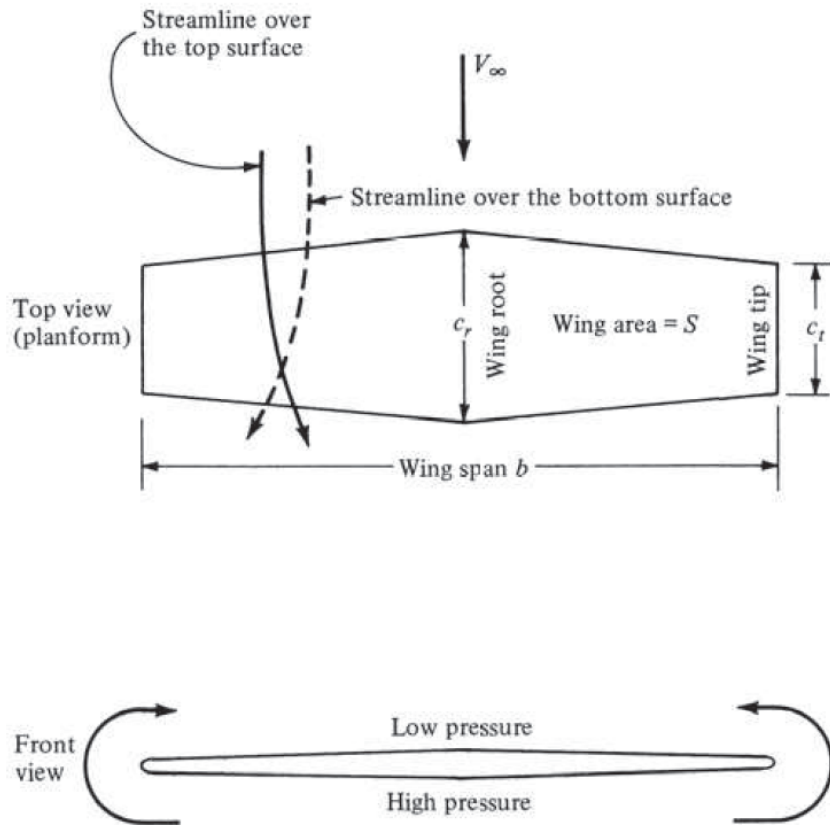


Figure 1: Finite wing flow pattern.
Fig 5.3 from reference [1]

These spanwise velocity components are the most intense close to the wingtips where the pressure imbalance resolves, but are present across the entirety of the wingspan. This contrast in direction of spanwise velocity components at the trailing edge creates a vortex sheet which sheds from the trailing edge and extends downstream[1, 9]. Figure 2 below shows the development of the vortex sheet from the trailing edge of a finite wing, curling up to form the two distinct vortex cores.

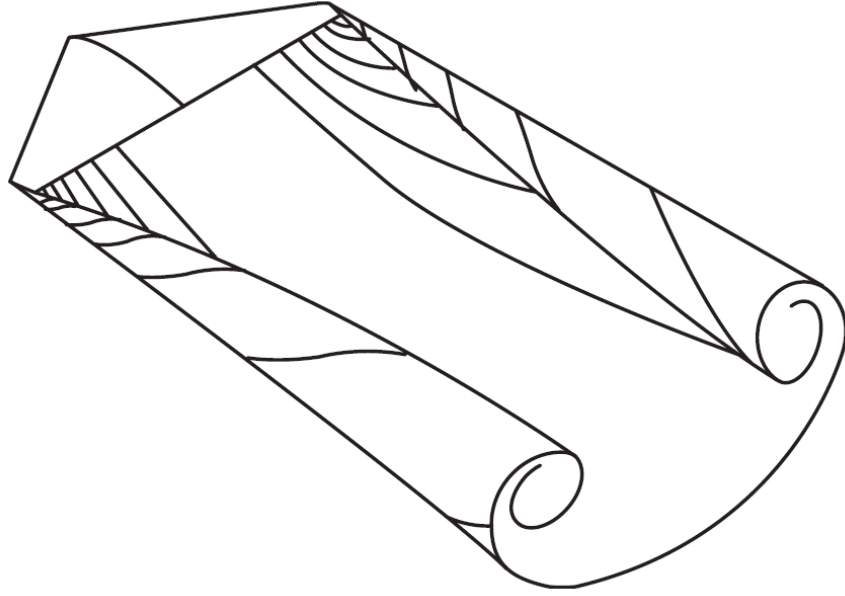


Figure 2: Vortex sheet development on a finite wing.
Fig 8.1.4 from reference [2]

This distribution of vorticity across the wing, which forms the vortex sheet, creates a downward component of velocity in the air that it passes through. This is called downwash, ω . Using Prandtl's Lifting Line Theory[10] and Biot-Savart law, the total downwash velocity induced at y_o by the vortex sheet can be calculated using equation 3[1]. Here, b is the aircraft span, y is the spanwise location, and Γ is the circulation over the wing.

$$\omega(y_0) = -\frac{1}{4\pi} \int_{-b/2}^{b/2} \frac{(d\Gamma/dy)dy}{y_0 - y} \quad (3)$$

This downwards velocity component, downwash, deflects the direction of the local flow of air in the vicinity of the wing downwards by an angle, the induced angle of attack, α_i . The induced angle of attack can be calculated using equation 4[1].

$$\alpha_i(y_0) = \tan^{-1} \frac{-\omega(y_0)}{V_\infty} \quad (4)$$

Because the local flow around the wing is inclined downwards through the induced angle of attack, α_i , the lift vector produced by the wing which is perpendicular to the local relative wind is tilted backwards in respect to the freestream velocity, V_∞ , through α_i .

With respect to the freestream velocity, this additional horizontal component of the lift vector from this rotation through α_i is the induced drag, D_i [1, 11]. This can be seen in Figure 3 below.

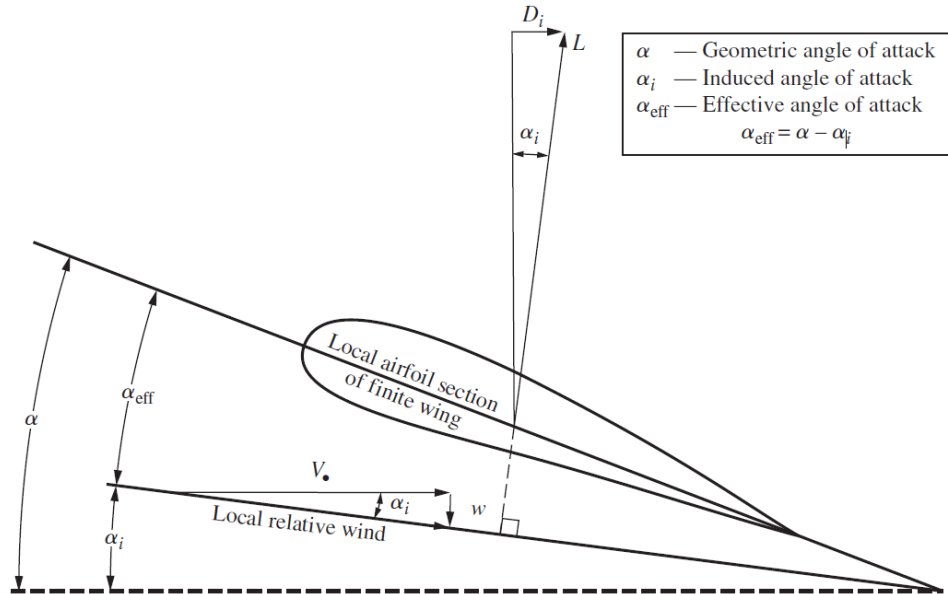


Figure 3: Diagram of induced drag
Fig 5.6 from reference [1]

1.3 Drag Reduction

There have been numerous innovations made in both aircraft design and manufacturing that reduce aircraft drag. Some have seen widespread deployment[12] where the additional costs often associated with these solutions are seen as worthwhile for the application of the aircraft. Such innovations include fairings[13], flush rivets[14], gap seals[15], spatted undercarriages and retractable landing gear[16, 17, 18], flap track fairings[12], and improved aerodynamic design of externally mounted components such as antenna covers, sensor housings and light fixtures. These innovations typically reduce the form drag component of the profile drag of an aircraft.

Other innovations have been proven effective, but the associated costs and added complexity that come as a consequence of their use has slowed their adoption in use on a larger scale. Such innovations include riblets[19] and hybrid laminar flow control[20, 21] (recently deployed in the vertical stabiliser on the Boeing 787 Dreamliner) which instead attempt to decrease the skin friction drag. Bleeding strategies have also been developed in which the body in flow introduces fluid into the wake. This increases the pressure of the wake, reducing the pressure difference between the wake and the freestream, and consequently the associated pressure drag[22, 23].

Morphing wing geometry has also long been developed and works by changing either the wing or airfoil shape in flight to adapt and better suit a variety of flight conditions, enhancing performance[24]. However, these systems are often very large, heavy and complex and to date have seen limited adoption, although further development continues.

One of the longest serving and simplest to implement means by which to reduce the drag of an aircraft is the use of a wingtip device, often a winglet or a wingtip fence. However, new concepts for wingtip devices continue to be innovated and developed.

1.4 Wingtip Devices

Wingtip devices reduce drag by altering the lift distribution over the wing in such a manner as to reduce the vorticity generated, reducing downwash and consequently induced drag.

Munk’s Stagger Theorem, which is derived and proven across pages 218 and 219 of *Theoretical Aerodynamics*, Milne-Thomson (1973)[9], states the following:

“The total induced drag of a multiplane system does not change when the elements are translated parallel to the direction of the wind provided that the circulations are left unchanged. Thus the total induced drag depends only on the frontal aspect.”

Consequently, the induced drag can be reduced by increasing the horizontal span, or vertical height of the lifting system[8, 9, 2]. A winglet and many other wingtip devices, such as wing fences, achieve the latter. However, the use of wingtip devices for these performance improvements come at the cost of increased weight. The additional weight from the wingtip device itself and its fittings contribute to this, but wingtip devices generally increase bending moments on the wing, which often results in a need for additional material to be used in the wing’s structural design[8]. Additionally, it is critical to ensure that any reduction in the induced drag of an aircraft through the use of such a wingtip device is not exceeded by an increase in the form drag which comes as a consequence of the added geometry of the wingtip device[25][8]. Many of the early attempts at designing wingtip devices to reduce induced drag were unable to consistently achieve this.

1.4.1 Early Development Of Wingtip Devices

As early as 1897 Frederick. W. Lanchester patented the use of vertical end plates at the tip of the wing, creating what is widely considered an early form of wingtip device[26]. He later published his work in *Aerodynamics* (1907)[27] in which they present wingtip vortices as the cause of induced drag[9]. This is not strictly correct inasmuch that as previously discussed the entire vortex sheet, not exclusively the wingtip vortices, is the cause of induced drag. However, it did pioneer the understanding between the vorticity produced (most obviously at the wingtips) and the induced drag of a wing.

In 1910 William E. Somerville filed a patent for a biplane flying machine in which the wingtips curl upwards akin to a modern winglet[28]. However, these early rudimentary designs often led to an increase in profile drag that surpassed any reduction in induced drag[8].

In 1918 Prandtl developed their lifting line theory which was subsequently developed on by their students, Betz, Trefftz, and Munk. Lifting line theory provides a model by which the induced drag can be calculated if the lift distribution is known[10].

There was some early effort made to assess the performance of wingtip devices by the National Advisory Committee for Aeronautics (NACA), notably Reid, E. G. in 1925[29], Hemke, P. E. in 1928[30] and Mangler, W. in 1938[31]. However, whilst these studies helped develop the understanding of induced drag, they showed that the increase in profile drag outweighed any benefit in the reduction of induced drag when using these early wingtip device designs.

After World War II, research into induced drag and designs to reduce it continued. In 1952 Dr Sighard F. Hoerner, working at Wright-Patterson Air Force base in the United States of America, wrote technical paper 52752, “*Aerodynamic Shape of Wing Tips*”. The paper demonstrated that sharp, round wingtips drawn back towards the trailing edge reduced induced drag[32]. Whilst Hoerner’s work did not result in the design of a wingtip device, it did further develop the understanding of induced drag and flow behaviour at the wingtip.

1.4.2 Development of Winglets

It was not until 1973 in the wake of the oil crisis that serious work was undertaken in the development of modern wingtip devices. The oil crisis had seen drastic increases in oil prices that caused many industries to start searching for energy-saving equipment to reduce their costs[33], including the aviation industry, in which the cost of fuel is a significant operational cost. Hence, a reduction in induced drag reduces fuel consumption and thus costs.

In 1976 Kichio Ishimitsu authored a paper for the American Institute of Aeronautics and Astronautics (AIAA) in which they detailed a procedure for the design and analysis of winglets utilising a Vortex Lattice Method (VLM) and use of Trefftz plane analysis. The paper showed that the theoretical results using this method closely matched experimental data from a Boeing 747 and a Boeing KC-135 aircraft. The paper also demonstrated that a 6.2% reduction in drag could be obtained through the use of a winglet[34]. That same year, Ishimitsu also published works in a collaboration between the Boeing Commercial Airplane Company and the United States Air Force on the design and analysis of winglets for military aircraft[35, 36].

In the same year, Richard T. Whitcomb working at the National Aeronautics and Space Administration (NASA) Langley Research Center published *Technical Note D-8260*, “*A Design Approach And Selected Wind-Tunnel Results At High Subsonic Speeds For Wing-Tip Mounted Winglets*”. Whitcomb’s work demonstrated the possibility of reaping the induced drag reduction whilst keeping the increased profile drag to a minimum through good aerodynamic design. Their study showed that the use of a winglet could produce twice the lift to drag ratio gain than an increase of wing span of equal added structural mass[25, 2, 37].

Quickly after Whitcomb’s work, many other studies were performed at NASA’s Langley Research Center to better understand the potential applications and optimize the efficiency of these winglets[38, 39, 40, 41, 42, 43, 44]. Notably, Heyson et al. produced *Technical Memorandum X-74003*[45], a parametric study of winglets and wing-tip extensions in 1977 which confirmed Whitcomb’s recommendations

and made efforts to optimize these winglet designs. Additionally, the following year in May 1978 Flechner and Jacobs produced *Technical Memorandum 72674* [46], which performed wind tunnel testing of winglets on scale models of jet aircraft. Their work demonstrated that the use of winglets did not produce any adverse effects on buffet onset, lateral stability, or aileron control effectiveness. As a result of their findings, flight-testing of winglets on a KC-135A for the following year was undertaken, which can be seen in Figure 4 below.



Figure 4: KC-135A Stratotanker flight testing winglets in 1979.
Image EC79-11314, Dryden Flight Research Center Photo Collection, NASA[3]

Following these developments, wingtip devices saw their first use in the airline industry. In 1985 the Airbus A310-300 was launched as the first airliner utilising wingtip fences, another type of wingtip device. Also in 1985 Boeing announced the 747-400, a variant of the 747 utilising winglets.



(a) Airbus A310-300 wingtip fence



(b) Boeing 747-400 winglet

Figure 5: Two images a and b showing some of the earliest commercial uses of wingtip devices on an Airbus A310-300 and Boeing 747-400 respectively.

Images courtesy of Adrian Pingstone

1.4.3 Modern Development Of Wingtip Devices

Since the introduction of the use of wingtip devices into the aviation industry, wingtip fences and winglets have emerged as the most commonly used. Consequently, there have been numerous efforts to optimise their designs for application across the commercial aviation industry[47, 48].

The clear benefits of the use of wingtip devices including winglets have led to their use and adoption in other industries, such as Unmanned Aerial Vehicles (UAVs)[49, 50], wind turbine blades[51, 52, 53] and competition sailplanes[54].

In 2001 Ilan Kroo[55] published a paper reviewing ideas and methods for induced drag prediction and reduction. They concluded that opportunities for new concepts of wingtip device remain, but serious challenges could be faced in attempting to integrate them with other aspects of the system.

New concepts for wingtip devices continue to be conceptualised and developed but are yet to see the widespread deployment that wingtip fences and winglets have. Such devices include spiroids[4], wing-grids[56], active wingtip devices[24] and ducted winglets[5].

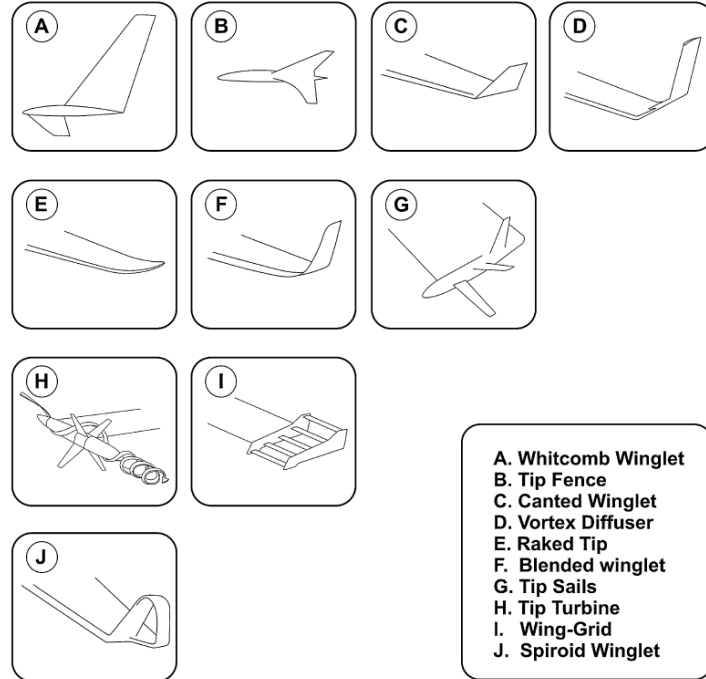


Figure 6: Wingtip devices currently in use or testing stage.

Fig 1 from reference [4]

1.4.4 The Ducted Winglet

The ducted winglet is a novel design for a wingtip device similar to a conventional winglet, but with a duct from the wing’s lower surface through to the tip of the winglet.

A patent filing for a ducted winglet design claims that the effect of the duct is to “*control the flow of air from the high-pressure (lower wing) surface to the lower pressure (upper wing) surface and so reduce the strength of wingtip vortices and thus the Induced Drag*” [5].

It is a common misconception that the vortices near the wingtips are condense flow phenomena which are the cause of vorticity throughout the flowfield and as a result, induced drag. Rather, they are much more disperse and manifest from the vorticity and conditions present in the larger flowfield, much like how the vortex sheet manifests as a result of the flowfield at the trailing edge, as previously discussed[8].

Below, Figure 7 shows a Figure from the aforementioned patent showing the duct, denoted by 428.

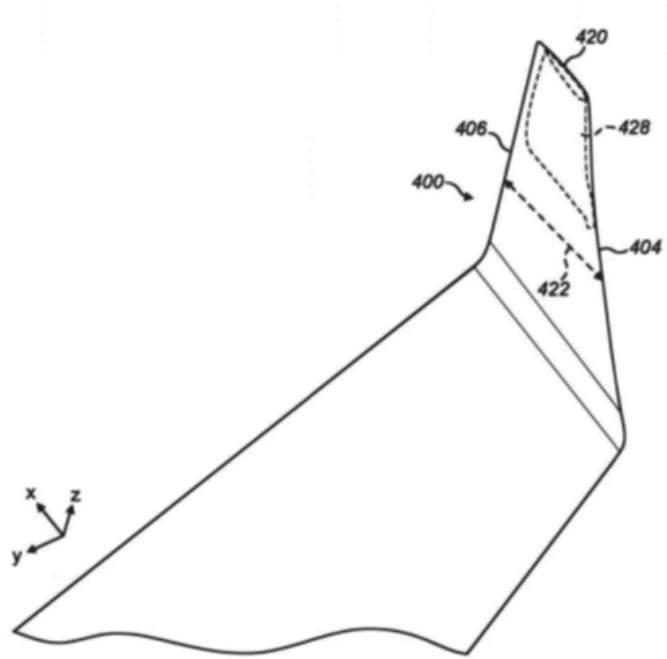


Figure 7: Figure from a patent for a ducted winglet design.
Fig 9 from reference [5]

1.5 Surface Integration and Far-Field Techniques

1.5.1 Surface Integration Techniques

Surface integration techniques are utilised by most Computational Fluid Dynamics (CFD) solvers, to determine the lift and drag forces. After a mesh has been developed to represent the body under study, the surfaces of the body are represented by a number of small faces, often called facets.

The sum of the components in the lift, drag and lateral directions of the normal and tangential forces, the pressure and skin friction forces respectively, acting on these facets determine the forces of lift, drag and lateral force. This method only allows for the calculation of the total drag, and does not provide a means to distinguish between the contributions made by profile drag and induced drag.

1.5.2 Far-Field Techniques

Far-field techniques were first developed theoretically in 1972 by Maskell[57]. This work was developed upon in 1985 when Brune and Hallstaff applied a far-field technique to experimental data gathered using a transonic wind tunnel. Measurements were taken using approximately 20,000 data points coincident on a plane perpendicular to the tunnel axis located approximately 2 chord lengths downstream of the trailing edge of the aircraft half model[58].

In 1992 Nikefrat et al. demonstrated the use of a far-field technique for the evaluation of aerodynamic drag from simulated flowfield solutions based on the Euler equations[59]. In their work, they showed how they were able to separate their drag into its two components, isolating a value for induced drag which cannot be achieved with surface integration techniques. As such, for evaluating the performance of a winglet, or any other wingtip device designed to reduce induced drag, a far-field technique must be chosen to allow for the decomposition of the total drag into its constituent parts such that the induced drag and performance of the wingtip device can be evaluated.

1.6 Trefftz Plane

Trefftz plane analysis is a momentum balance far-field wake integral technique in which a plane is taken downstream of the body under study and has been used extensively to assess the performance of wingtip devices and their effect on induced drag[34, 47, 60]. Integration of the perturbation velocities squared, where the perturbation velocities are the velocity components perpendicular to the freestream, over the area of this plane derives the induced drag. It is critical to ensure that when applying this method that the plane is perpendicular to the freestream and that the plane is large enough to capture all perturbations.

The equation for this integration can be seen in equation 5[61]. Here D_i is the induced drag, ρ is the freestream fluid density, S_T is the Trefftz plane, \hat{v} and \hat{w} are the vertical and horizontal velocity perturbations on the Trefftz plane respectively, and \hat{u} is the velocity perturbations in the freestream direction.

$$D_i = \frac{1}{2} \rho \iint_{S_T} (\hat{v}^2 + \hat{w}^2 - \hat{u}^2) dS \quad (5)$$

Using equation 1 and the solution of equation 5, the coefficient of induced drag can be derived, as seen below in Equation 6.

$$C_{D_i} = \frac{2 D_i}{\rho V_\infty^2 A} \quad (6)$$

2 Hypothesis

This paper will investigate the hypothesis that a ducted winglet may offer a performance advantage over a conventional winglet of the same outer geometry. It is hypothesised that due to the air passing through its duct, a ducted winglet may effectively act as though it were a conventional winglet of increased length; changing the local flow field in the same manner as a longer conventional winglet, offering a performance increase without the additional mass costs that a larger winglet would present. It is important to note that this hypothesis does not explore the idea that the wingtip vortex can be controlled or straightened out. As Doug McLean, a retired Boeing Technical Fellow, eloquently states, “*Even if a device eliminates the vorticity from the streamtube that passes through its inlet, compensating vorticity is generated and shed from the external surfaces of the device. Unless the overall distribution of lift on the wing is changed, the total vorticity and the global flow pattern are substantially unchanged.*” [8].

This project explores the hypothesis by comparing the performance of a ducted winglet, a conventional winglet of the same outer geometry, and a standard wingtip across a range of angles of attack in a computational fluid dynamics CFD study.

3 Model Development

3.1 Geometry

This project utilised three different geometric configurations in its study, a Ducted Winglet (DW), a Conventional Winglet (CW) of the same outer geometry, and a Standard Tip (ST). These wingtip geometries can be seen in Figure 8.

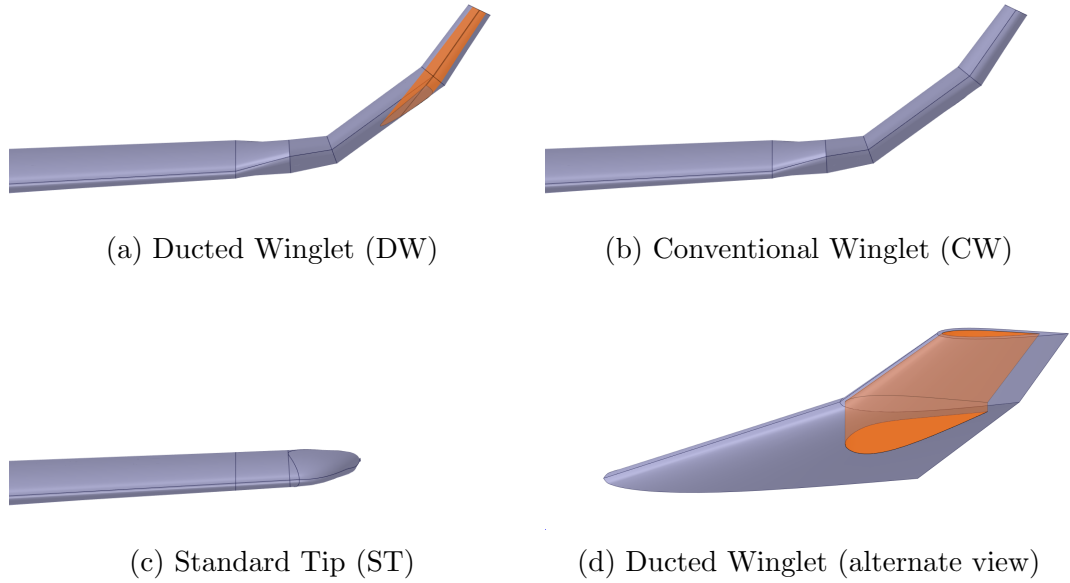


Figure 8: Three images, a, b, c, showing the ducted winglet, conventional winglet and standard tip geometries respectively from the leading edge. A fourth image, d, shows the ducted winglet from the wingtip. Interior duct surfaces highlighted orange.

Each wingtip configuration was modelled onto a half model of a Embraer ERJ145, a regional twin turbofan engine aircraft. The half model does not have vertical or horizontal stabilisers, this can be seen later in fig 11. This model was provided to the author and has been used previously in the study of induced drag reduction wingtip devices. As discussed in section 1.2 induced drag is a product of any lifting system and as such the omission of the non-lifting surface of the vertical stabiliser should have little to no effect on the induced drag.

There are countless potential horizontal stabiliser configurations. A horizontal stabiliser can be configured to produce positive lift, negative lift, or no lift at

all. Additionally, horizontal stabilisers are often mounted to the fuselage at a different angle of incidence to that of the main wing. Consequently, inclusion of the horizontal stabiliser could have obscured the effect of the ducted winglet on the main wing and made it harder to have established an understanding of its effects, as this project attempts to do. However, the main wing is the primary lifting surface and as such produces the most induced drag. Additionally, it is the effect of the application of the ducted winglet to the main wing that this project investigated.

A half model was used, as under Steady, Level, Unaccelerated Flight (SLUF) conditions the flowfield can be considered symmetric about the plane of geometric symmetry down the longitudinal axis of the aircraft. This allows for a more efficient use of computational resources, as the computational resources needed to complete a CFD simulation is proportional to the number of cells in the mesh being run. A half model allows for a mesh of twice the cell density than a whole model mesh to be run at practically no extra computational cost.

The geometry for the ducted and conventional winglets were created using SOLIDWORKS 2021, a computer aided design Computer Aided Design (CAD) software. The outer geometry for each winglet is identical and closely follows that laid out by the aforementioned patent[5]. The ducted variant has a channel comprised of two sections. The first extends from the winglet tip to the offset profile of the airfoil at the bend of the winglet. The second section extends perpendicular from this profile, through to the underside of the wing.

The half models of the Embraer ERJ145 with each wingtip configuration were used to create the computational domain, the volume in which the flow of air is simulated in a CFD study. The size of the domain extends +/- 150 m in the z-axis, +/- 350 m in the x-axis, and from 0 m to + 150 m in the y-axis.

In the domain, the half model of the Embraer ERJ145 lies with the axis of its fuselage collinear with the x-axis, and the nose of the aircraft positioned at $x = 0$ m. The plane of symmetry of the aircraft lies on the xz plane at $y = 0$ m such that the one symmetric half model of the aircraft lies in the domain.

As established in section 1.6, the Trefftz plane method requires that all velocity perturbations are captured by the Trefftz plane. Consequently, the domain sizing must be large enough such that velocity perturbations are only present on the downstream face of the domain.

The values of the domain were approximately determined by using a common rule of thumb by extending the domain an order of magnitude away from the aircraft. To do this, the domain was extended symmetrically along each cardinal axis. For the x-axis, the domain was extended such that each face was 11 fuselage lengths from the origin. For the y and z axes, the domain was extended such that each face was 11 wing spans from the origin. The domain was then extended further such that all faces excluding the plane of symmetry were located a distance from the origin rounded up to the nearest 50 m increment.

Solutions from the mesh independence study showed that the domain was sufficiently large enough that velocity perturbations were only present on the downwards face. The results of the Trefftz plane analysis shown later in section 4.2.1 and appendix 9.2 that the domain sufficiently captures the velocity perturbations. An isometric view of this geometry can be seen in Figure 9.

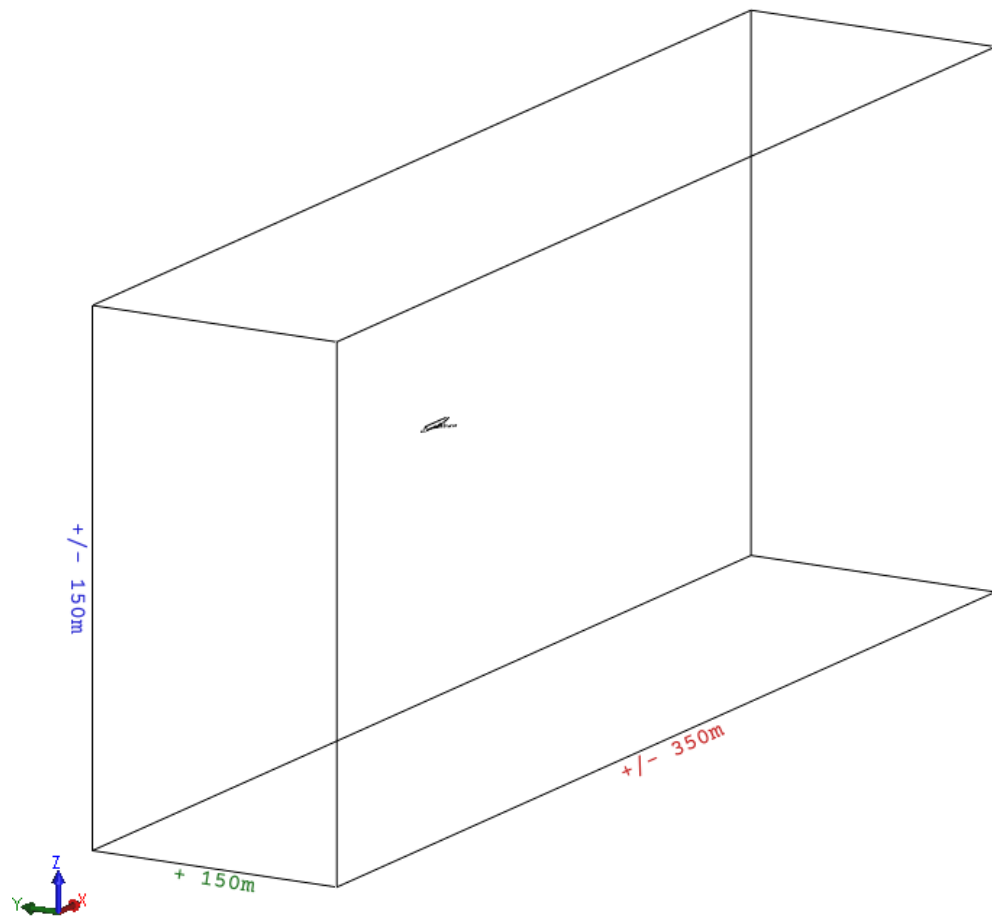


Figure 9: Isometric view of model geometry and far-field fluid domain.

3.2 Flight Conditions

The flight conditions used in the CFD study as seen in Table 1 were selected as they are emblematic of those that are typically experienced by an Embraer ERJ145 aircraft, the aircraft used for the base geometry of the model[62].

The CFD study was performed using these flight conditions at increments of 1° through the range of angles of attack. Note abbreviation, Reynolds Number (Re).

Table 1: Flight conditions

Flight Condition	Value
Altitude	30,000 ft
Velocity	236.46 m/s
Mach	0.78
Re	17,500,000
Angle of Attack (α)	$0^\circ \geq \alpha \geq 5^\circ$
Air Density	0.01503 Kg/m ³

Consequently, performing CFD simulations for each of the 3 different geometries at each angle of attack resulted in a total of 18 simulations that were performed. The coefficients of both the total drag and induced drag were found for each solution. This was done for the assessment and evaluation of the performance of each geometry configuration at each increment across the range of angles of attack.

3.3 Mesh Generation

This domain was populated with an unstructured tetrahedral mesh generated using the FLITE Mesh Generation suite, an open-source surface and volume meshing software that was developed by the Zienkiewicz Centre for Computational Engineering at Swansea University[63].

An unstructured mesh was chosen as it allows the changing of mesh element sizing in desired locations. This facilitated the optimisation of computational resource into better solving volumes of complex flow by ensuring finer cells are present in these locations, whilst cells grow coarser where freestream conditions are present.

The FLITE Mesh Generation suite utilises Delaunay triangulation and allows the user to define point, line and plane sources for mesh control. The one, two and three points used to define each of these sources respectively are defined by the user. At each point defined, the user defines an inner radius (r_1) within which the mesh is composed of elements under a maximum element size (E_{max}) which the user also defines. The cells then grow from this inner radius to an outer radius (r_2) which is also defined, where the cell sizing limitation matches that of the global value or any other constraint enforced upon that volume.

The buffer volume between the two radii ensures a smooth transition between the desired cell sizing restriction and the cell sizing outside this radius, keeping the volume ratio between cells as low as possible across this transition, which benefits the quality of the mesh[64].

Use of these point, line and plane sources allow for great control over the mesh generation and were used to ensure that areas of complex flow had high mesh density. Areas upstream or away from the aircraft in the freestream were allowed to grow to a lower mesh density to optimise the computational resources available to the areas in the domain of particular interest.

3.3.1 Mesh Independence Study

A mesh independence study was conducted to establish confidence that the results of the computational fluid dynamics studies were conducted to a sufficient level of accuracy, and optimise the computational resources available. This study was performed using the model for the conventional winglet using the flight conditions described in section 3.2 at 2 degrees angle of attack.

Cell sizing constraints were placed along the aircraft fuselage, leading edge, trailing edges, and at the wingtip of the aircraft. Additionally, a conical shaped constraint was implemented across all meshes to ensure a higher mesh density would be present where the vortex core would form downstream of the wingtip however the cell sizing for this remained consistent for all meshes.

The radii of the cell sizing constraints were kept constant throughout the mesh independence study, however the inner radius cell sizing constraint was changed between meshes. The cell sizing information used in the mesh independence study can be seen in Table 2 below.

Table 2: Mesh independence study parameters.

Mesh Constraint Source (m)	Mesh						
	1	2	3	4	5	6	7
Wingtip	0.2	0.1	0.05	0.025	0.015	0.015	0.0175
Nose	0.5	0.25	0.1	0.1	0.05	0.05	0.035
Fuselage	1	0.5	0.1	0.1	0.05	0.05	0.035
Leading Edge	0.5	0.25	0.2	0.15	0.125	0.025	0.02
Trailing Edge	0.5	0.25	0.2	0.15	0.125	0.025	0.02

The results from the mesh independence study can be seen in Figure 10 and Table 3.

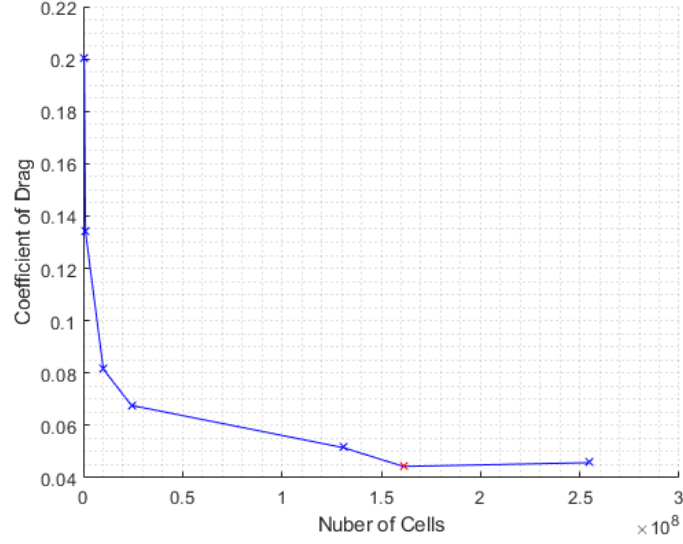


Figure 10: Mesh independence study results.

Table 3: Mesh independence study

Number of Cells	Coefficient of Drag
520533	0.200380
1110252	0.134150
10108880	0.081490
24299737	0.067641
130763166	0.051560
161242332	0.044327
254637119	0.045787

As can be seen in Figure 10 and Table 3, the mesh independence study converged at the sixth mesh (highlighted in red) and as such it was this mesh configuration that was utilised for the simulations in this project.

3.3.2 Final Mesh

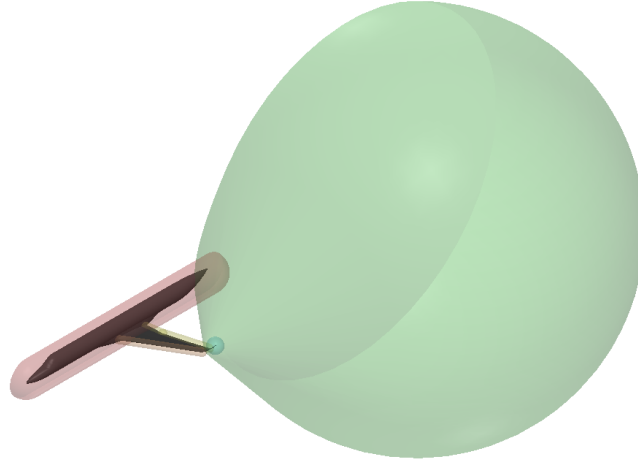
The final mesh configuration chosen contained approximately 160 million cells, approached convergence after running for 12 days (288 hours) on 128 Central Processing Unit (CPU) cores, and was selected to be used for the CFD studies.

The locations, types, and parameters used to control the unstructured mesh in the final mesh configuration can be seen in Table 4. Note abbreviations, Leading Edge (LE) and Trailing Edge (TE).

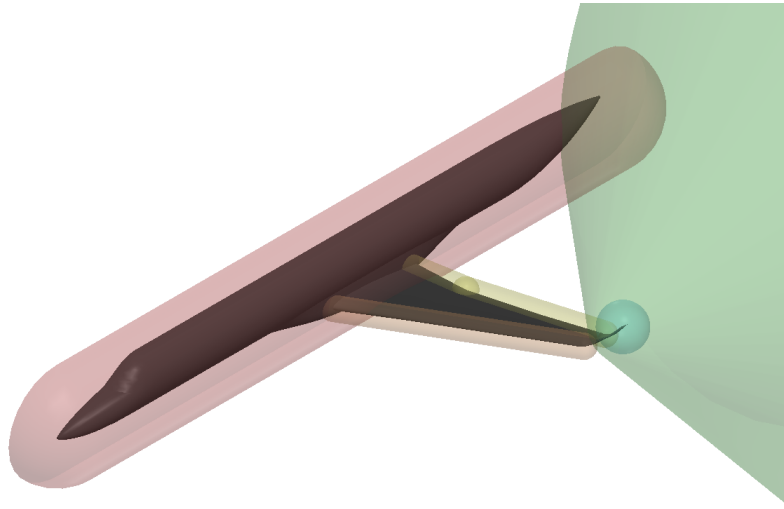
Table 4: Final mesh properties of sources for cell sizing constraint

Source	Location	X (m)	Y (m)	Z (m)	E_{max} (m)	r_1 (m)	r_2 (m)
Point	Wingtip	18.829	-10.395	-0.052	0.015	1.5	2.0
Line	Fuselage	0.000	0.000	0.000	0.050	0.5	5.0
Line	Fuselage	28.000	0.000	0.000	0.050	0.5	5.0
Line	LE	13.172	-1.101	-1.006	0.025	0.5	1.0
Line	LE	17.469	-9.799	-0.511	0.025	0.5	1.0
Line	TE 1	17.202	-1.087	-1.183	0.025	0.5	1.0
Line	TE 1	17.338	-3.815	-0.902	0.025	0.5	1.0
Line	TE 2	17.338	-3.815	-0.902	0.025	0.5	1.0
Line	TE 2	18.552	-9.799	-0.511	0.025	0.5	1.0
Line	Vortex	18.829	-10.395	-0.052	0.500	1.5	2.5
Line	Vortex	50.000	-10.395	-0.052	0.500	25.0	50.0

The areas of mesh constraint used in the final mesh can be seen in Figure 11, with each area of constraint identifiable by their respective colour displayed in Table 4.



(a) Zoomed out



(b) Zoomed in

Figure 11: Two images a and b showing zoomed in and zoomed out views respectively of the Embraer ERJ145 geometry with mesh constraints.

3.3.3 Inflation Layers

The FLITE Mesh Generation suits also allows the user to define inflation layers. These are very thin layers of cells shaped as triangular prisms extending from the surface of the body under study, into the unstructured mesh. The purpose of these inflation layers are to better capture the behaviour of the flow in the boundary layer.

The values used to define these inflation layers can be seen in Table 5 below, and the selection of these values is discussed throughout this section.

Table 5: Properties of inflation layers

Property	Value	Unit
First Layer Thickness	5.4e-6	m
Number of Inflation Layers	50	-
Growth Ratio	1.2	-
Last Layer Thickness	0.041	m
Total Thickness	0.248	m

Using the Reynolds number Re equation, equation 7, the Reynolds number can be calculated. Here ρ is the fluid density, V is the fluid velocity, L is the reference length and μ is the dynamic viscosity of the fluid.

$$Re = \frac{\rho V L}{\mu} \quad (7)$$

Using the mean aerodynamic chord as the reference length, the values in Table 1 and information from the International Standard Atmosphere the other terms can be found and the Reynolds number can be calculated to approximately 17,500,000.

With a value for the Reynolds number calculated and the mean aerodynamic chord length of the aircraft, an approximate value for the boundary layer thickness on the wing of the aircraft can be found using Schlichting's equation for turbulent boundary layer thickness along a flat plate channel, equation 8. Here, x is the distance downstream from the start of the boundary layer for which the previously

used value of the mean aerodynamic chord is used, Re is the previously calculated value of Reynolds number, and $\delta(x)$ is the calculated height of the boundary layer.

$$\delta(x) \approx 0.37 \frac{x}{Re_x^{1/5}} \quad (8)$$

Following this method returns an admittedly approximate value of 0.032 m for the boundary layer thickness on the wing, under the aforementioned flight conditions. This is well below the total thickness of the inflation layers, which as can be seen in Table 5 has a value of 0.248 m, ensuring that the inflation layers capture the boundary layer flow in its entirety.

As previously stated, keeping the volume ratio between cells as low as possible is ideal and often used as an indicator of the quality of a mesh[64]. Consequently, the inflation layers have been allowed to keep expanding at a growth ratio of 1.2 until a final layer thickness of 0.041 m. This minimises the volume ratio between this final inflation layer thickness and the mesh cell sizing enforced outside the boundary layer. In Table 4 it can be seen that whilst excluding the refinement sources associated with the trailing vortex, the largest value of the maximum element sizing control, E_{max} , is 0.05 m. Consequently, the effective growth ratio between the last inflation layer and the freestream is reduced to approximately 1.22.

Figure 12 shows the inflation layers growing in a structured grid away from the aircraft body (coloured blue) into the freestream, where the mesh becomes unstructured. It can be seen that the final inflation layer cell sizing is very close to that of the closest cells of the freestream.

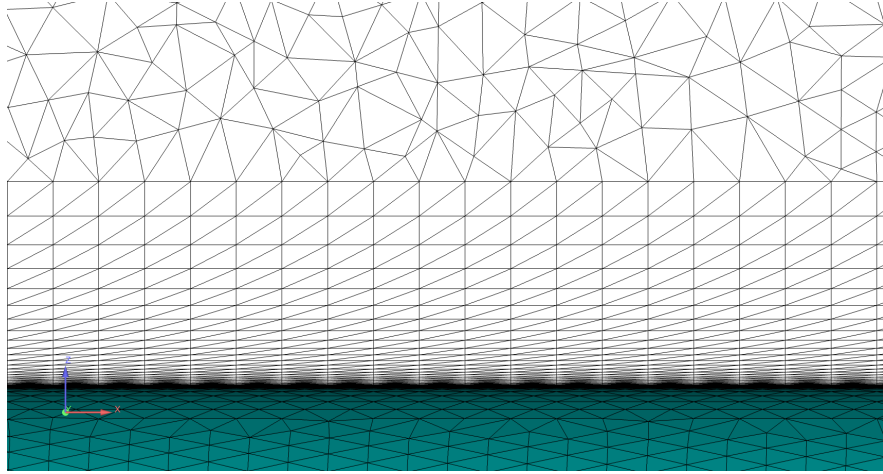
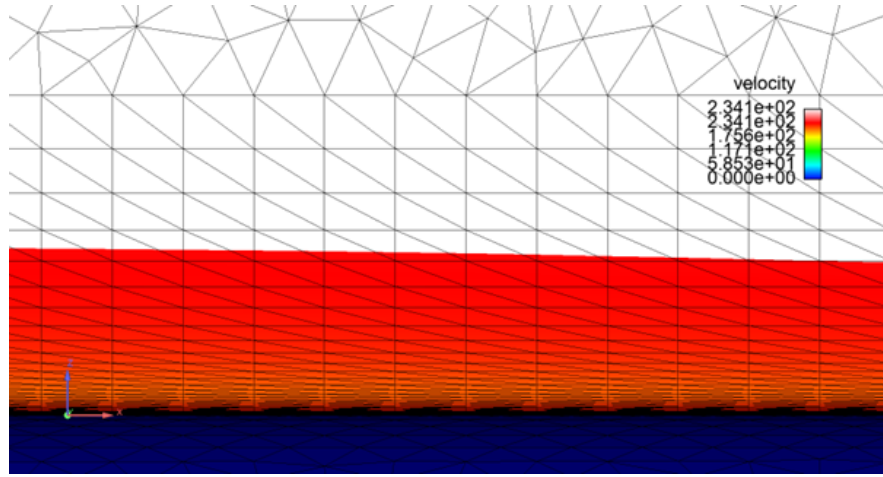


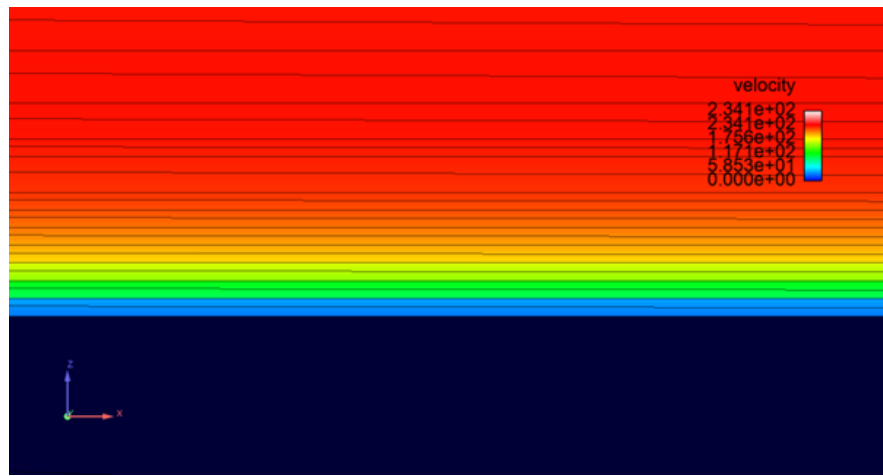
Figure 12: Inflation layers growing from aircraft body into freestream.

Figure 13a below shows the boundary layer, which is defined as 99% of the freestream velocity. It is coloured by its velocity magnitude, with values exceeding the boundary layer flow velocity coloured white to clearly show the extent of the boundary layer. It can be seen that the boundary layer is captured by the structured inflation layers before reaching the unstructured freestream mesh in laminar flow.

Figure 13b shows the no-slip condition is present as the aircraft body surface shows a velocity of 0 m/s with the air velocity increasing quickly as distance from the surface also increases.



(a) Inflation layers capturing boundary layer thickness in laminar flow.



(b) Inflation layers capturing boundary layer velocity gradient.

Figure 13: Two images a and b showing the boundary layer flow in the inflation layers and those closest to the surface respectively.

3.4 CFD Solver

The FLITE3D[65] CFD solver developed by the department of Aerospace Engineering at Swansea University was selected for use in running the CFD study. FLITE3D is a nodal-based Reynolds Averaged Navier-Stokes (RANS)[66] flow solver that has been used substantially in the research community[67, 68].

The one-equation Spalart-Allmaras turbulence model[69] was utilised with FLITE3D to produce a viscous compressible steady state solution. The Spalart-Allmaras model has been used extensively in industry and research in aerodynamic CFD applications since its introduction in 1992[70].

The FLITE3D CFD solver utilises a first order upwind discretisation of the partial differential equation used in the Spalart-Allmaras equation[71] similar to the approach that which was used in the original Spalart-Allmaras paper[69].

The FLITE3D solver utilises a surface integration method for the calculation of the lift and drag, as described in section 1.5.1. This allowed for the FLITE3D solver to provide the total lift and drag, and their coefficients, but could not separate the drag into its constituent components of profile drag and induced drag.

3.4.1 Boundary Conditions

Boundary conditions were specified for the fluid domain for its use in FLITE3D. These can be seen below in Figure 14.

All surfaces making up the geometry of the aircraft (coloured blue in Figure 14) were flagged such that when volume meshing, inflation layers would grow from these surfaces[72] and during the simulation would follow the no slip condition.

The boundary lying on the xz plane (coloured green in Figure 14) was flagged as a plane of symmetry and as such after surface meshing the mesh on this surface was changed to allow for the inflation layers that would grow coincident to the plane away from the aircraft body surfaces[72].

All other surfaces (coloured red or hidden in Figure 14) were flagged as far-field surfaces. After surface meshing, these surfaces aren't changed[72]. The fluid at these surfaces are consistent with the relevant values from Table 1 unless flow phenomena in the simulation changes them.

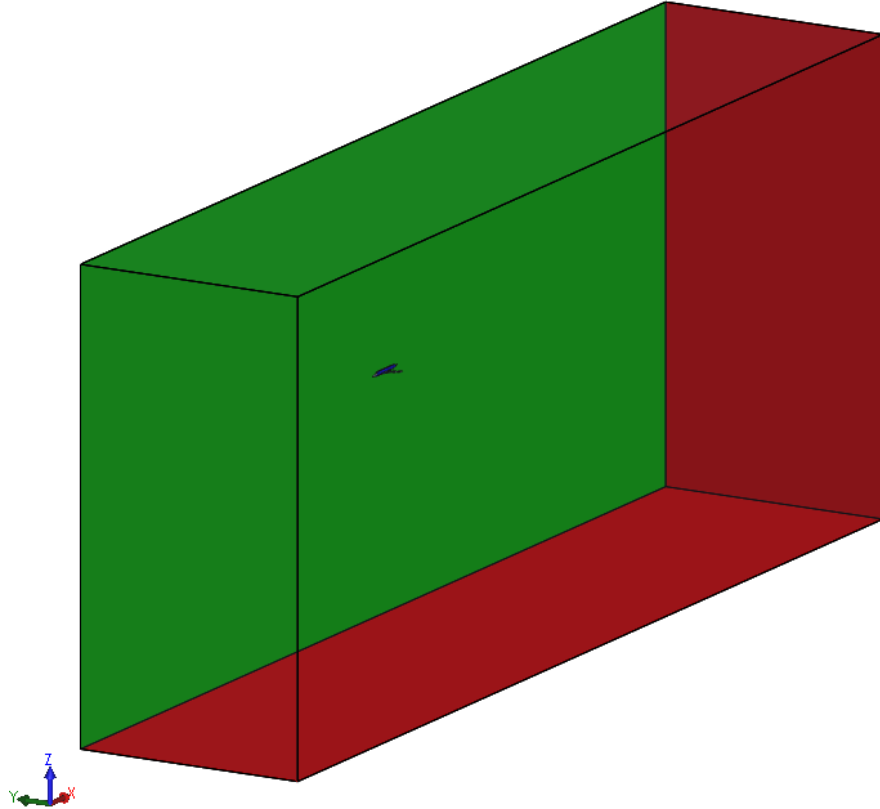


Figure 14: Boundary conditions on domain.

3.5 Hardware And Other Software

The computational work utilised by this project in meshing, pre-processing and running the Computational Fluid Dynamics software was performed on Swansea University’s Impact High Performance Computing (HPC) cluster running a Linux terminal environment. Results from the CFD solver, FLITE3D, are output in an EnSight GOLD format. At the time of this study, the Impact HPC cluster did not have a licence for ANSYS EnSight, a post-processing tool that the format was developed for. Consequently, post-processing of the computational fluid dynamics results was performed on the author’s personal computer using ANSYS EnSight student edition.

The use of the author’s personal computer for post-processing results introduced challenges concerning computational resource limitations. The principle challenge being that the EnSight GOLD format files output by the FLITE3D CFD solver were larger than the Random Access Memory (RAM) available on the author’s personal computer. Consequently, a fork of the FLITE3D solver was created in which the Fortran code was edited to output a formatted EnSight GOLD solution, rather than a binary EnSight GOLD solution. This allowed the author to develop a MathWorks MATLAB code which when deployed to the Impact HPC could open these files, import the data, and exclude the information pertaining to the geometry, density, energy and velocity of the unstructured mesh outside a specified volume. This volume could be defined as either a point source and radius, or the space between two yz planes at different x-axis positions. This reduced the file size sufficiently that the author could then open the EnSight GOLD files on their personal computer, but limited the post-processing opportunities to smaller volumes within the domain. As such, much of the post-processing performed was limited to the wingtip itself, or a plane perpendicular to the freestream as shall be discussed in a later section.

4 Analytical Methodology

This project utilised several different methods of analysis to evaluate the performance of the ducted winglet and the alternate geometries used for comparison.

These include:

- Surface integration drag coefficient calculation
- Far-field Trefftz plane induced drag coefficient calculation
- Velocity mapping on plane through the winglet duct

What follows in this section is a discussion on the methods listed above, their selection, implementation and the theory behind these choices.

4.1 Surface Integration

As described in section 3.4, the FLITE3D CFD solver utilises a surface integration technique as detailed in section 1.5 to derive the lift and drag forces and their coefficients.

Whilst winglets and other wingtip devices work by reducing the induced drag, it is important to also ensure that the benefit of this reduction in induced drag is not outweighed by the cost of additional profile drag, as was the case with early wingtip device concepts[8]. As such, when assessing the performance of a wingtip device, it is important to also consider the total drag, not only the induced drag in isolation. To this end, the values for the coefficient of drag calculated by FLITE3D for the ducted winglet, conventional winglet and standard tip, across all values of angle of attack used in this study are collected and presented in the results, in section 5.

4.2 Far-Field Trefftz Plane

As discussed previously in section 1.6, the Trefftz plane is a momentum balance far-field wake integral method which can be used to calculate the induced drag of an aircraft. It forms the primary method of analysis used in this project. With the exception of the near-field, the Trefftz plane can be theoretically located anywhere downstream from the body provided that the plane is large enough to capture all the velocity perturbations. The near-field is typically defined using equation 9[60], where x is the downstream position from the leading edge and c is the chord length.

$$x/c \approx 10 \tag{9}$$

Within this near-field volume the flow is more prone to modelling errors due to the steep velocity gradients and pressure thrust and viscous stress forces are prominent in the wake. Outside the near-field these pressure thrust and viscous stress components of the wake tend to negligible values, whilst only the momentum component remains[60, 73], allowing for the use of the Trefftz plane method.

In inviscid flow, the Trefftz plane is taken far downstream of the body under study, as the perturbations in the freestream direction must die away[61]. This allows for the simplification of equation 5 and the much more common form of the Trefftz plane method seen below in equation 10.

$$D_i = \frac{1}{2} \rho \iint_{S_T} (\hat{v}^2 + \hat{w}^2) dS \tag{10}$$

However, this project modelled viscous flow in its CFD solutions and as such equation 5 where the \hat{u} term, representing perturbations in the freestream direction is present, had to be used.

$$D_i = \frac{1}{2} \rho \iint_{S_T} (\hat{v}^2 + \hat{w}^2 - \hat{u}^2) dS \tag{5 revisited}$$

Trefftz plane analysis of induced drag has widely been used in research for a number of different flow regimes, including transonic flow[74].

The data of the flow solutions is contained in the nodes of the unstructured mesh, which grows from a finer resolution around the areas of mesh constraint to a coarser resolution as described in section 3.3. Therefore, as the mesh resolution decreases moving further away from the areas of mesh constraint, so does the resolution of information pertaining to the velocity perturbations[75, 60]. Consequently, the Trefftz plane was placed at $x = 45$ m, where $x/c \approx 11$. This places the Trefftz plane outside the near-field volume downstream of the trailing edge, but relatively close to the aircraft, where the mesh is at its most dense. This can be seen in Figure 15.

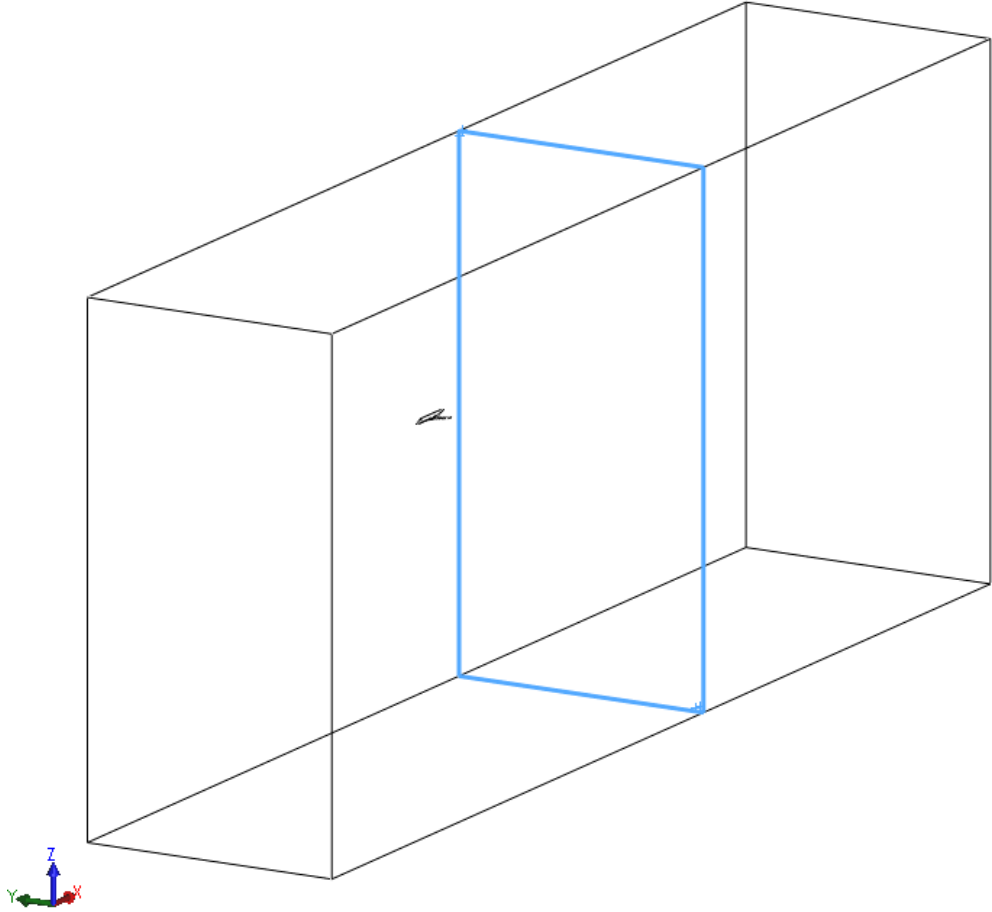


Figure 15: Isometric view of Embraer ERJ145 geometry and far-field fluid domain, the Trefftz plane, in blue.

4.2.1 Software Implementation Of The Trefftz Plane Method

Once results were obtained for each wingtip configuration and angle of attack combination, they were opened with ANSYS EnSight, a post-processing tool. In this software, the Trefftz plane was introduced through the fluid volume.

An example of a plane taken aft of the aircraft, viewed from downstream, can be seen in Figure 16. Figure 16 also shows cuboid patterns present in the volume mesh at the periphery of the areas of mesh restrain detailed in section 3.3.2 where they meet the freestream. This is an artefact of the element break method utilised by the FLITE3D mesh generation suite in the creation of the volumetric mesh. Additionally, in Figure 16 it can be seen that the further the cells are from the centre of the right-hand side, where the Embraer ERJ145 is located and consequently the areas of mesh refinement defined in Table 4, the size of the elements grows larger and therefore the data resolution decreases.

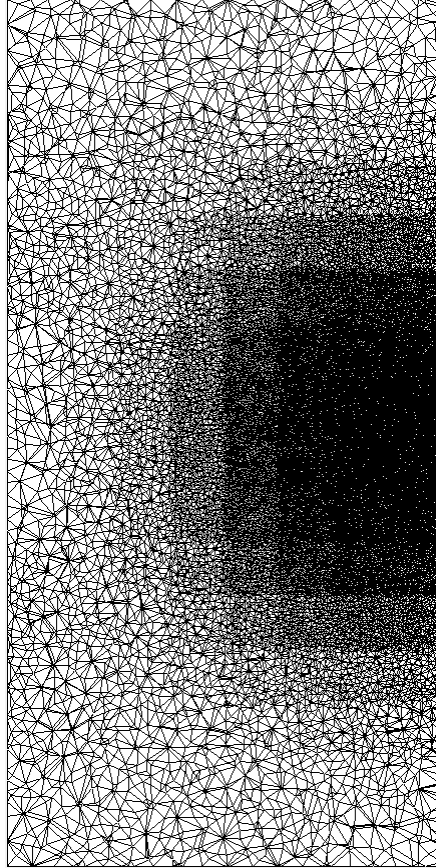


Figure 16: Mesh on Trefftz plane at $x = 45$ m

When first introduced into ANSYS EnSight the results are nodal based, meaning that information is stored at the nodes of the unstructured mesh rather than the mesh cells. However, as the areas defined by the intersection of the Trefftz plane and each cell it passes through are used in the scripted implementation of the Trefftz plane described shortly, this information was converted from being nodal based to element based. These conversions were achieved using inbuilt utilities in ANSYS EnSight. The information on these planes were exported from ANSYS EnSight as a flatfile.

A MathWorks MATLAB script, available in appendix A, section 9.1, was developed capable of importing these flatfiles, performing the Trefftz plane method calculation in equation 5, and carrying out other post-processing activities.

An example of the Trefftz Plane analysis post-processing output by this script can be seen in Figure 17. In this figure we can also see the degradation in the resolution of the data where the mesh is coarser as previously discussed. All such Trefftz Plane post-processed outputs are available in Appendix B, section 9.2.

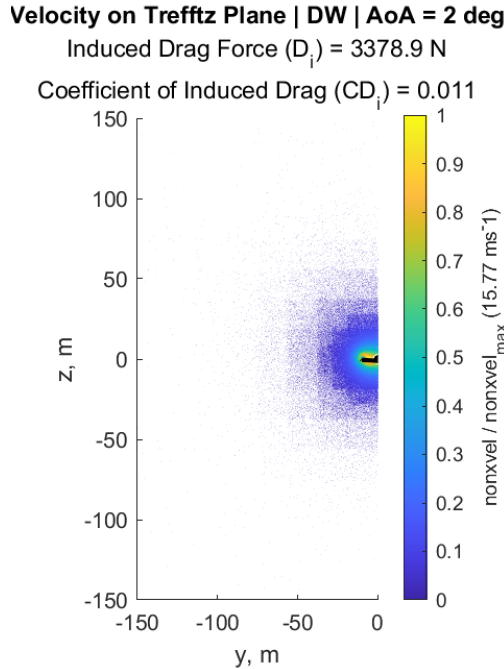


Figure 17: Example MathWorks MATLAB Trefftz Plane analysis output

A semicircle and pair of lines are superimposed over the velocity vectors to show the profile of the fuselage and trailing edge, respectively. This can be seen more clearly in Figure 18, where the axes have been restricted to $-25m \leq y \leq 0m$ and $-22.5m \leq z \leq 22.5m$.

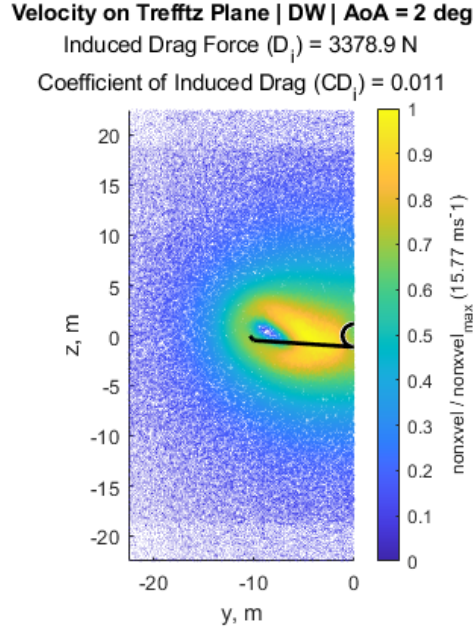


Figure 18: Example MathWorks MATLAB Trefftz Plane analysis output zoomed in

Once again, the cuboid patterns present in the volume mesh at the periphery of the areas of mesh control can be seen. These results output by the MATLAB code show the velocity parallel to the Trefftz plane. The velocity vectors are coloured using a scale also shown. The scale ranges from a minimum value of 0 m/s to a maximum value of the maximum velocity parallel to the Trefftz plane, which is shown in parentheses for each case.

The total calculated induced drag force and the coefficient of induced drag are also shown alongside information detailing the geometry and angle of attack configuration present.

4.3 Path Lines

ANSYS EnSight was used to perform some additional post-processing, including the use of path lines to show the flow of the air ejected from the outlet at the tip of the ducted winglet. This was achieved by introducing a plane just upstream of the duct opening, from which the path lines followed the flow downstream. These path lines were coloured using the velocity of the flow.

The results of this post-processing performed on the ducted winglet at each angle of attack can be seen in appendix C, section 9.3. An example of this can be seen in Figure 19 below.

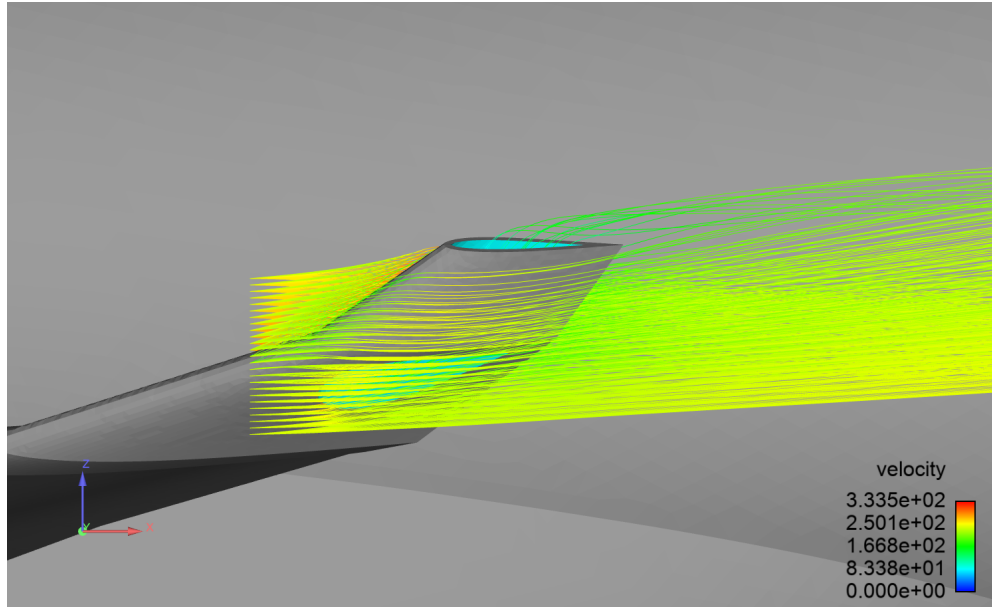


Figure 19: DW path lines at angle of attack = 0

It can be seen that the interior surfaces of the duct are coloured cyan, whilst all others are coloured grey to ensure that they are visibly distinct.

4.4 Velocity Planes

Additional post-processing was performed using ANSYS EnSight on the flow solutions of the ducted winglet cases to develop an understanding of the flow through the duct.

A plane, defined by 3 points, was taken through the flow of the duct. The three points used to define this plane were located at the leading edge of the duct outlet, the trailing edge of the duct outlet, and the trailing edge of the duct inlet. This resulted in a plane intersecting the flow through the entirety of the length of the duct. These planes were then coloured using the velocity range local to the plane.

The results from this post-processing can be seen in appendix D, section 9.4. It should be noted that the views depicted are not normal to this plane, but in the -Y direction. An example of this can be seen in Figure 20 showing the flow through the duct at 0° angle of attack.

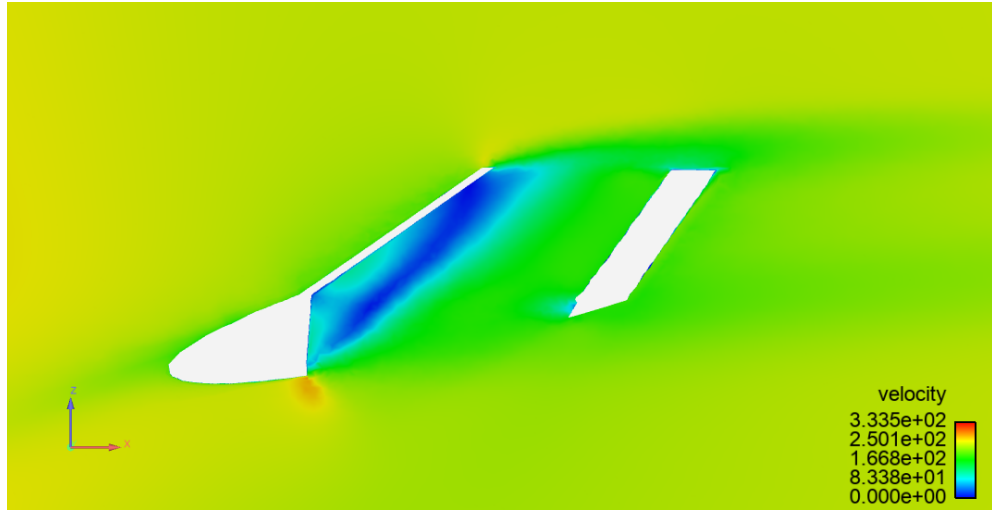


Figure 20: Duct velocity on plane at angle of attack = 0

An alternate form of these planes were also generated where instead of colouring the plane using the velocity, the plane itself was coloured grey and velocity vectors originating on the plane were plotted and coloured using the same range of velocities local to the plane. These planes can be seen in appendix E, section 9.5, with an example shown below in Figure 21, again at 0° angle of attack.

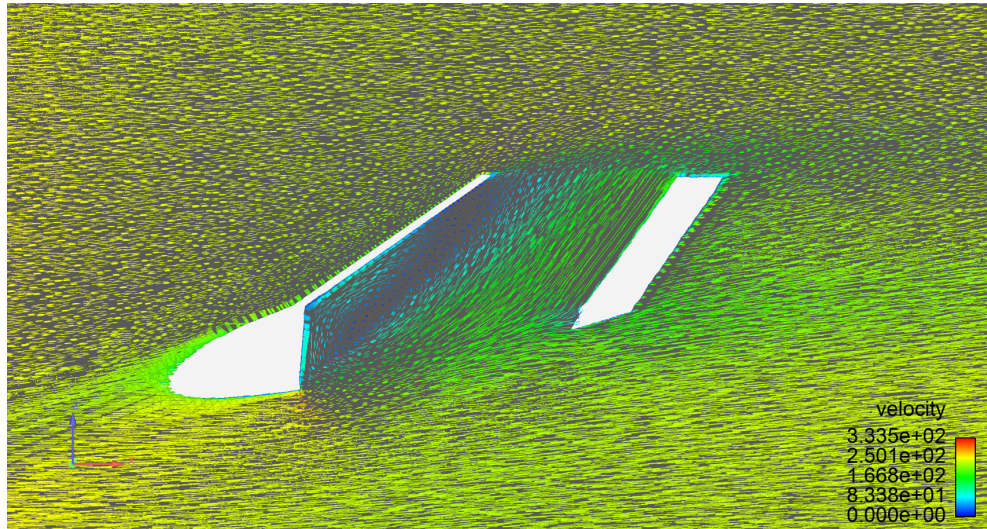


Figure 21: Duct velocity vectors on plane at angle of attack = 0

5 Results

5.1 Accuracy and Uncertainty

As previously stated in the final mesh discussion, section 3.3.2, the unstructured mesh for each wingtip configuration consisted of approximately 160 million cells and solutions were run for 12 days (288 hours) on 128 CPU cores, for a total of 36,864 CPU hours per solution. Across the three different geometries, each tested across six different angles of attack, 663,552 CPU hours in total were utilised in the study. This excludes the CPU hours spent generating the meshes, pre-processing each solution, and performing the mesh convergence study.

An example of the convergence of the coefficient of drag for the conventional winglet at 5 degrees angle of attack can be seen in Figure 22 below. A figure showing convergence for all studies is presented in appendix F, section 9.6.

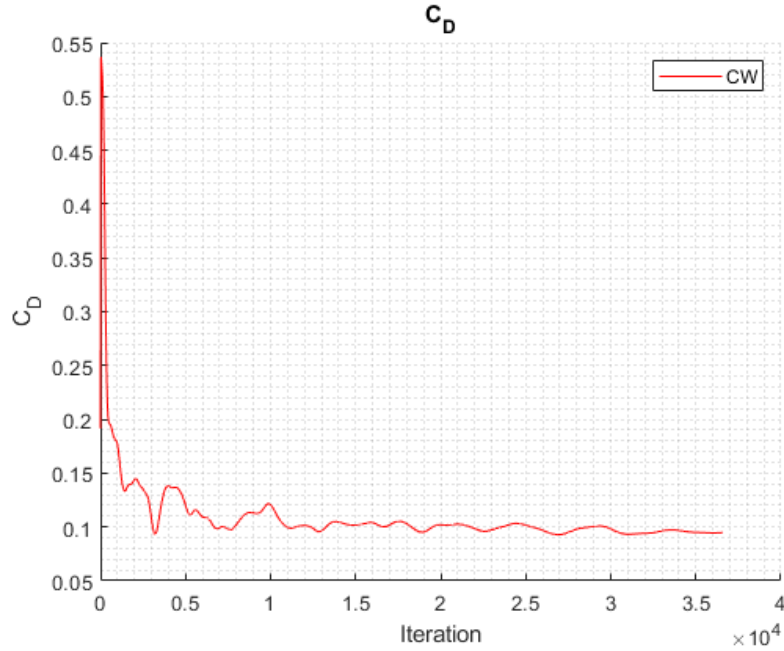


Figure 22: Example of convergence of C_D

As can be seen, the solution converged quickly to an approximate value after 10000 iterations, and converged on a final solution shortly after 35000 iterations. Similar behaviour was seen for the solutions at other angles of attack in the study.

In addition to the results being run until they established convergence, it should be noted that the patterns of performance between the geometry configurations were quickly established and held for the vast majority of the duration of the simulations. Therefore, when comparing the performance of the different wingtip geometry configurations, whilst the differences are often small in value, they are nonetheless well established.

This can be seen in Figure 23 below, in which a portion of the C_D convergence spanning several thousand iterations at approximately midway through the simulations for the cases at 5° angle of attack is shown. It can be seen that even this early into the convergence of the solutions that whilst the results fluctuate slightly, they do so in parallel after the pattern of performance between the different wingtip geometries was well established.

Thus, whilst results given in the following sections are to an extreme number of significant figures, this is to better show the magnitude of these often very small but very well established patterns of behaviour between the wingtip configurations that could easily diminish considerably with rounding error.

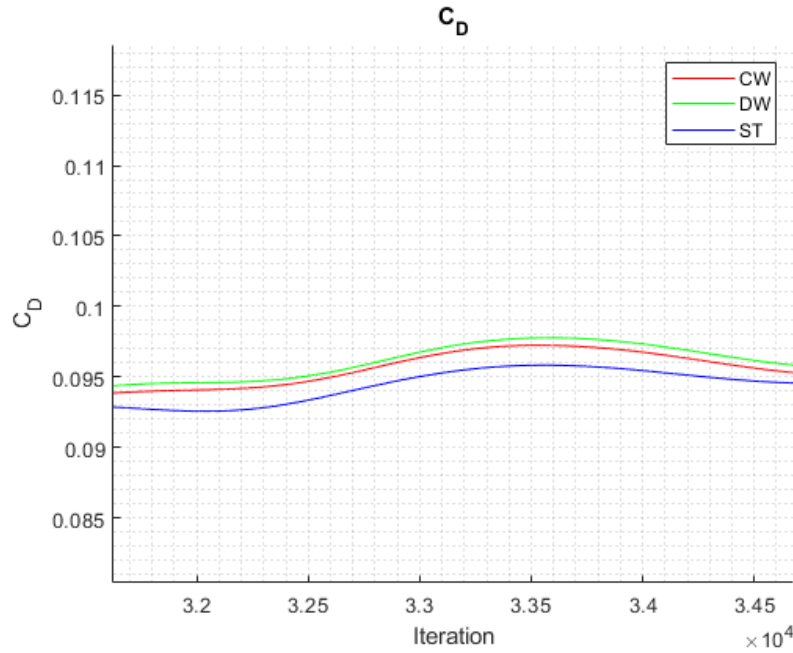


Figure 23: Example of pattern of performance established in convergence of C_D across all wingtip geometries.

5.2 Surface Integration Coefficient Of Drag Results

Results from the surface integration technique in the FLITE3D solver produced the values for the coefficient of drag as seen in Table 6 and Figure 24.

Table 6: Surface Integration FLITE3D C_D results

Angle of Attack (Deg)	C_D		
	CW	DW	ST
0	0.0284	0.0280	0.0284
1	0.0343	0.0333	0.0341
2	0.0443	0.0441	0.0439
3	0.0595	0.0596	0.0594
4	0.0763	0.0773	0.0764
5	0.0949	0.0953	0.0947

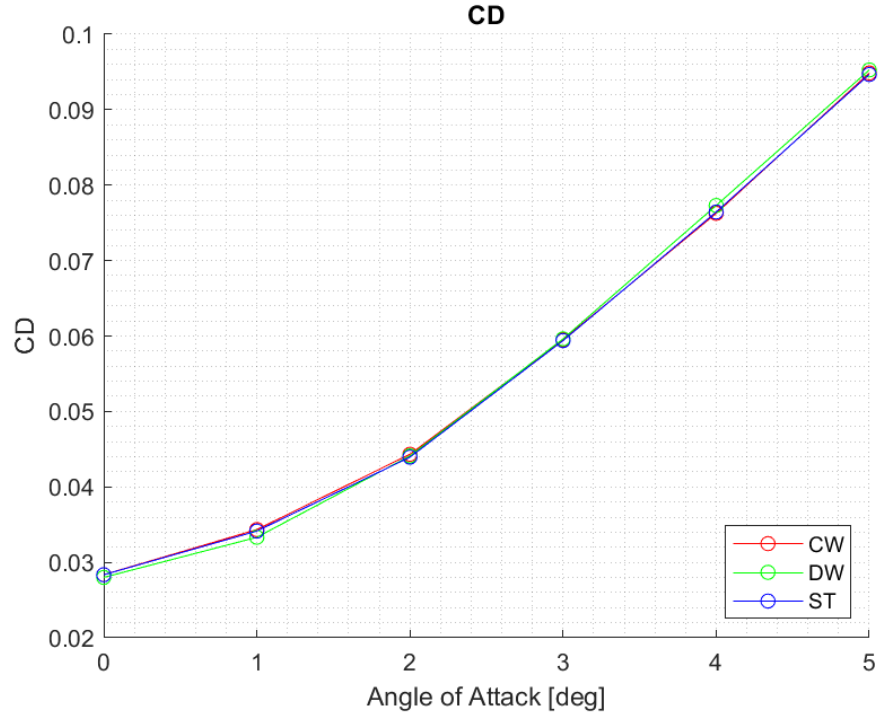


Figure 24: C_D values for each geometry at each angle of attack

5.3 Far-Field Coefficient Of Induced Drag Results

Using the flowfield data from these steady state solutions, a plane was introduced downstream at a location of $x = 45$ m, where equation 9 is satisfied. This plane was used to employ the Trefftz plane far-field technique as described in section 4.2 to determine the coefficient of induced drag. These results can be seen in Table 7 and Figure 25.

Table 7: Far-field Trefftz plane analysis C_{D_i} results

Angle of Attack (Deg)	C_{D_i}		
	CW	DW	ST
0	0.0039	0.0038	0.0040
1	0.0073	0.0071	0.0074
2	0.0108	0.0106	0.0111
3	0.0147	0.0143	0.0150
4	0.0180	0.0178	0.0183
5	0.0210	0.0206	0.0215

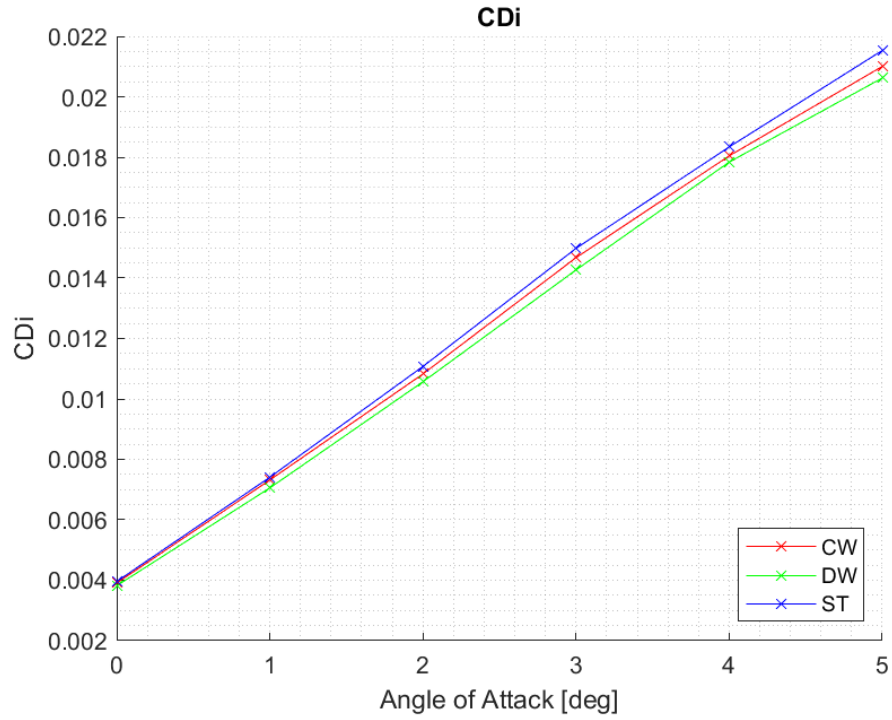


Figure 25: C_{D_i} values for each geometry at each angle of attack

5.4 Discussion

As can be seen in Table 7 and Figure 25 in section 5.3, across all cases the conventional winglet produced a lower coefficient of induced drag than the standard tip, and the ducted winglet produced even lower values than the conventional winglet. On average, the conventional winglet produced values of coefficient of drag approximately 1.8% lower than that of the standard tip, whilst the ducted winglet produced values of 4.2% lower than the standard tip.

Whilst these savings are lower than the 6.2% saving shown by Ishimitsu's 1976 study[34] these savings are nonetheless consistently observed across all angles of attack, showing the clear performance benefit that the ducted winglet offers. Additionally, it is probable that this difference can in part be accounted for by the fact that both the conventional and ducted winglet geometries used in this study were produced by the author and not by an aircraft design and manufacturing company such as Boeing.

Table 6 and Figure 24 in section 5.2 show that whilst the performance of the conventional and ducted winglets closely match that of the standard tip at lower angles of attack, they both produced higher values than the standard tip at higher values of angle of attack.

As can be seen in Figures 20 and 21 and those in appendices D and E, sections 9.4 and 9.5, a large portion of the flow in the duct has very low velocity. This is seen starting at the leading edge of the inlet, on the lower side of the wing, throughout the duct to the leading edge of the outlet. This volume of low velocity flow in the duct is present in all ducted winglet cases regardless of the angle of attack, and clearly a consequence of the geometry of the duct through the winglet.

It can be seen in Figure 21 and those in appendix 9.5, by use of the velocity vectors, that the airflow eddies after the sharp corner of geometry at the entrance of the inlet. Additionally, it can be seen that there is a volume of high velocity flow from the point of separation at the leading edge of the duct inlet.

Figure 19 and those in appendix C, section 9.3, show air being ejected through the outlet of the duct at the tip of the winglet to some height before becoming

laminar with the freestream flow further downstream. This is the type of behaviour that the ducted winglet was hypothesised to produce.

It is clear that future iterations of ducted winglets should better ensure that the freestream flow can be introduced into the duct without causing the flow to eddy or separate at the leading edge of the duct inlet. The presence of the eddy reduces the total velocity of the flow through the duct and hinders the benefit of the ducted winglet, which is dependent on the exhausted flow and its velocity.

6 Conclusion

This paper utilised FLITE3D, a Reynolds Averaged Navier-Stokes computational fluid dynamics solver using a Spalart-Allmaras turbulence model and unstructured meshes to simulate flows around a ducted winglet, conventional winglet and standard wingtip geometry configurations across a range of angles of attack.

The FLITE3D solver derived the total drag of each geometry and angle of attack combination using a surface integration method. A momentum balance far-field Trefftz plane method was used to derive the induced drag from these flow fields to assess the efficiency of each geometry and angle of attack combination. It was established using these methods that across all angles of attack, the ducted winglet reduced the induced drag. However, at angles of attack above 1° the total drag produced by the ducted winglet exceeded that of the other wingtip geometries.

Use of velocity planes through the duct of the winglet show that the two-sectioned design of the duct used in this project causes the flow to separate on entry into the duct and eddy. The presence of the eddy reduces the total velocity of the flow through the duct and hinders the benefit of the ducted winglet, which is dependent on the exhausted flow and its velocity. It is clear that future iterations of ducted winglets should better ensure that the freestream flow can be introduced into the duct without causing the flow to eddy.

In conclusion, whilst it has been shown that whilst a ducted winglet design reduces induced drag, there are still optimisations that can be made in the design of the ducted winglet.

The author believes that a recommendation similar to that made by Whitcomb in 1976 can be made inasmuch that there is the potential to reduce induced drag using a ducted winglet style design. However, to achieve this, good aerodynamic design must be followed to ensure that this benefit is not offset by an increase in form drag.

7 Future Work

It is the author's recommendation that future work relating to a ducted winglet style of wingtip device includes a parametric investigation into the design of the duct to better optimise the ducted winglet for the chosen flight conditions and continue to develop the understanding surrounding the wingtip device.

Additionally, particular care should be given to the design and creation of the geometry around the inlet and interior channel of the duct. This is to ensure that the freestream flow is introduced into the duct as smoothly as possible, thus avoiding the eddying behaviour as seen on the velocity planes through the duct used in this study.

Lastly, studying the effect and behaviour of the ducted winglet at different flight conditions, including those typical at take-off and landing, would be beneficial for further developing the understanding of the performance of the ducted winglet in practical operation.

8 Bibliography

References

- [1] Anderson J.D. *Fundamentals of Aerodynamics*. McGraw-Hill, 2017. ISBN 978-1-259-25134-4.
- [2] McLean D. *Understanding Aerodynamics: Arguing The Real Physics*. Wiley, 2016. ISBN 978-81-265-6031-8.
- [3] NASA. Ec79-11314, dryden flight research center photo collection, nasa, 1979. URL <https://www.nasa.gov/centers/dryden/multimedia/imagegallery/KC-135/EC79-11314.html>.
- [4] Guerrero J. E., Maestro D., and Bottaro A. Biomimetic spiroid winglets for lift and drag control. *Comptes Rendus Mécanique*, 340(1-2):67–80, 2012. doi: <https://doi.org/10.1016/j.crme.2011.11.007>.
- [5] Smith J. J. Wo 2018/130612 a1, 2018. URL <https://patents.google.com/patent/W02018130612A1>.
- [6] Gunston B. *The Cambridge Aerospace Dictionary*. Cambridge University Press, 2011. ISBN 978-0-511-63403-1.
- [7] Clancy L.J. *Aerodynamics*. Pitman, 1978. ISBN 0-273-01120-0.
- [8] McLean D. Wingtip devices: what they do and how they do it. In *Boeing performance and flight operations engineering conference*, 2005.
- [9] Milne-Thomson L. M. *Theoretical aerodynamics*. Courier Corporation, 1973. ISBN 978-0-486-61980-4.
- [10] Prandtl L. and Tietjens O. *Applied Hydro-and Aero-mechanics*. McGraw-Hill, 1934.
- [11] Anderson J.D. *Introduction to Flight*. McGraw-Hill, 2012. ISBN 978-981-4636-18-6.
- [12] Rudolph P. K. C. High-lift systems on commercial subsonic airliners. Technical Report CR-4746, NASA, 1996.
- [13] Hoerner S. F. *Fluid-Dynamic Drag*. Hoerner Fluid Dynamics, 1965.
- [14] W. G. Vincenti. Technological knowledge without science: The innovation of flush riveting in american airplanes, ca. 1930-ca. 1950. *Technology and Culture*, 25(3):540–576, 1984. ISSN 0376-0421. doi: <https://doi.org/10.2307/3104204>. URL <https://www.jstor.org/stable/3104204>.
- [15] A. Kowalska and T. Goetzendorf-Grabowski. Impact of the aileron gap sealing on the aileron effectiveness. *Aircraft Engineering and Aerospace Technology*, 95(1):26–37, 2023. ISSN 0002-2667. doi: <https://doi.org/10.1108/AEAT-01-2022-0001>. URL <https://www.emerald.com/insight/content/doi/10.1108/AEAT-01-2022-0001/full/html>.

- [16] W. H. HerrNSTein and Biermann D. The drag of airplane wheels, wheel fairings, and landing gears - i. Technical Report TR-485, NACA (NASA), 1935.
- [17] W. H. HerrNSTein and Biermann D. The drag of airplane wheels, wheel fairings, and landing gears - ii : Nonretractable and partly retractable landing gears. Technical Report TR-518, NACA (NASA), 1936.
- [18] W. H. HerrNSTein and Biermann D. The drag of airplane wheels, wheel fairings, and landing gears - iii. Technical Report TR-522, NACA (NASA), 1936.
- [19] Walsh M. J. Riblets for aircraft skin-friction reduction, ntrs:19880005573. In *Langley Symposium on Aerodynamics*, volume 1, pages 557–571, 12 1986.
- [20] Krishnan K. S. G., Bertram O., and Seibel O. Review of hybrid laminar flow control systems. *Progress in Aerospace Sciences*, 93:24–52, 2017. ISSN 0376-0421. doi: <https://doi.org/10.1016/j.paerosci.2017.05.005>. URL <https://www.sciencedirect.com/science/article/pii/S0376042117300404>.
- [21] Young T. M., Humphreys B., and Fielding J. P. Investigation of hybrid laminar flow control (hlfc) surfaces. *Aircraft Design*, 4(2):127–146, 2001. ISSN 1369-8869. doi: [https://doi.org/10.1016/S1369-8869\(01\)00010-6](https://doi.org/10.1016/S1369-8869(01)00010-6).
- [22] C. J. Wood. The effect of base bleed on a periodic wake. *The Aeronautical Journal*, 68(643):447–482, 1964. doi: <https://doi.org/10.1017/S036839310007989X>. URL <https://www.cambridge.org/core/journals/aeronautical-journal/article/abs/effect-of-base-bleed-on-a-periodic-wake/FDCA60C635BBA671AB71D150540765DE>.
- [23] P. W. Bearman. The effect of base bleed on the flow behind a two-dimensional model with a blunt trailing edge. *Aeronautical Quarterly*, 18(3):207–224, 1967. doi: <https://doi.org/10.1017/S0001925900004212>. URL <https://www.cambridge.org/core/journals/aeronautical-quarterly/article/abs/effect-of-base-bleed-on-the-flow-behind-a-twodimensional-model-with-a-blunt-trailing-edge/5159818B53BEC023D527BA2EC8450416>.
- [24] Sun J., Du L., Scarpa F., Liu Y., and Jinsong L. Morphing wingtip structure based on active inflatable honeycomb and shape memory polymer composite skin: A conceptual work. *Aerospace Science and Technology*, 106:541, 111, 4 2021. ISSN 1270-9638. doi: <https://doi.org/10.1016/j.ast.2021.106541>.
- [25] Whitcomb R. T. A design approach and selected wind-tunnel results at high subsonic speeds for wing-tip mounted winglets. Technical Report TN-D-8260, NASA, 1976.
- [26] Lanchester F. W. Gb189703608a, 1897. URL <https://patents.google.com/patent/GB189703608A/>.
- [27] Lanchester F. W. *Aerodynamics*. A. Constable and co., ltd., 1907.

- [28] Somerville W. E. Us1154214a, 1910. URL <https://patents.google.com/patent/US1154214A/>.
- [29] Reid E. G. The effects of shielding the tips of airfoils. Technical Report TR-201, NACA (NASA), 1925.
- [30] Hemke P. E. Drag of wings with end plates. Technical Report TR-267, NACA (NASA), 1928.
- [31] Mangler W. The lift distribution of wings with end plates. Technical Report TM-856, NACA (NASA), 1938.
- [32] Hoerner S. F. *Aerodynamic Shape of Wing Tips*, 52752. United States Air Force, 1952.
- [33] Burns A. F. Statement by arthur f. burns, chairman, board of govenors of the federal reserve system before the joint economic committee, november 27, 1974, 1974.
- [34] Ishimitsu K. K. Aerodynamic design and analysis of winglets. In *AIAA Aircraft Systems and Technology Meeting*, 1976. doi: <https://doi.org/10.2514/6.1976-940>.
- [35] Ishimitsu K. K. et al. Design and analysis of winglets for military aircraft. phase i. Technical Report AFFDL-TR-76-6, United States Air Force Flight Dynamics Laboratory and Boeing Commercial Airplane Company, 1976.
- [36] Ishimitsu K. K. et al. Design and analysis of winglets for military aircraft. phase ii. Technical Report AFFDL-TR-77-23, United States Air Force Flight Dynamics Laboratory and Boeing Commercial Airplane Company, 1976.
- [37] Zhang L., Ma D., Yang M., and Wang S. Optimization and analysis of winglet configuration for solar aircraft. *Chinese Journal of Aeronautics*, 33 (12):3238–3252, 12 2020. doi: <https://doi.org/10.1016/j.cja.2020.04.008>.
- [38] Flechner S. G., Jacobs P. F., and Whitcomb R. T. A high subsonic speed wind-tunnel investigation of winglets on a representative second-generation jet transport wing. Technical Report TN-D-8264, NASA, 1976.
- [39] Jacobs P. F. and Flechner S. G. The effect of winglets on the static aerodynamic stability characteristics of a representative second generation jet transport model. Technical Report TN-D-8267, NASA, 1976.
- [40] Jacobs P. F., Flechner S. G., and Montoya L. C. Effect of winglets on a first-generation jet transport wing. i - longitudinal aerodynamic characteristics of a semispan model at subsonic speeds. Technical Report TN-D-8473, NASA, 1977.
- [41] Montoya L. C., Flechner S. G., and Jacobs P. F. Effect of winglets on a first-generation jet transport wing. ii - pressure and spanwise load distributions for a semispan model at high subsonic speeds. Technical Report TN-D-8474, NASA, 1977.

- [42] Montoya L. C., Jacobs P. F., and Flechner S. G. Effect of winglets on a first-generation jet transport wing. iii - pressure and spanwise load distributions for a semispan model at mach 0.30. Technical Report TN-D-8478, NASA, 1977.
- [43] Jr Meyer R. R. Effect of winglets on a first-generation jet transport wing. iv - stability characteristics for a full-span model at mach 0.30. Technical Report TP-1119, NASA, 1978.
- [44] Jacobs P. F. Effect of winglets on a first-generation jet transport wing. v - stability characteristics of a full-span wing with a generalized fuselage at high subsonic speeds. Technical Report TP-1163, NASA, 1978.
- [45] Heyson H. H., Riebe G. D., and Fulton C. L. Theoretical parametric study of the relative advantages of winglets and wing-tip extensions. Technical Report TM-X-74003, NASA, 1977.
- [46] Flachner S. G. and Jacobs P. F. Experimental results of winglets on first, second, and third generation jet transports. Technical Report TM-72674, NASA, 1978.
- [47] Pfeiffer N. J. Numerical winglet optimization. aiaa 2004-213. In *42nd AIAA Aerospace Sciences Meeting and Exhibit Conference*, 2004. doi: <https://doi.org/10.2514/6.2004-213>.
- [48] Belferhat S., Meftah S. M. A., Yahiaoui T., and Imine B. Aerodynamic optimization of a winglet design. *EPJ Web of Conferences - EFM12 – Experimental Fluid Mechanics 2013*, 45, 2013. doi: <https://doi.org/10.1051/epjconf/20134501010>.
- [49] Panagiotou P., Kaparos P., and Yakinthos K. Winglet design and optimization for a male uav using cfd. *Aerospace Science and Technology*, 39:190–205, 12 2014. doi: <https://doi.org/10.1016/j.ast.2014.09.006>.
- [50] Weierman J. and Jacob J. D. Winglet design and optimization for uavs. In *28th AIAA Applied Aerodynamics Conference*, 2010. doi: <https://doi.org/10.2514/6.2010-4224>.
- [51] Elfarra M. A. *Horizontal axis wind turbine rotor blade: winglet and twist aerodynamic design and optimization using CFD*. PhD thesis, Middle East Technical University, 2011.
- [52] Benjanirat S. *Computational studies of horizontal axis wind turbines in high wind speed condition using advanced turbulence models*. PhD thesis, Georgia Institute of Technology, 2007.
- [53] Imamura H., Hasegawa Y., and Kikuyama K. Numerical analysis of the horizontal axis wind turbine with winglets. *JSME International Journal Series B*, 41(1), 2 1998. doi: <https://doi.org/10.1299/jsmeb.41.170>.
- [54] Maughmer M. D. The design of winglets for high-performance sailplanes. aiaa 2001-2406. In *19th AIAA Applied Aerodynamics Conference*, 1976. doi: <https://doi.org/10.2514/6.2001-2406>.

- [55] Kroo I. Drag due to lift: Concepts for prediction and reduction. *Annual Review of Fluid Mechanics*, 33(1):587–617, 2001. doi: 10.1146/annurev.fluid.33.1.587.
- [56] La Roche U. and Palffy S. Wing-grid, a novel device for reduction of induced drag on wings. In *Flow Control*. International Council of Aeronautical Sciences, 1996.
- [57] Maskell E. C. Progress towards a method for the measurement of the components of the drag of a wing of finite span. Technical Report 72 232, Royal Aircraft Establishment, 1972.
- [58] Brune G. W. and Hallstaff T. H. Wing span loads of complex high-lift systems from wake measurements. *Journal of Aircraft*, 22(9):831–832, 1985. doi: <https://doi.org/10.2514/3.45211>.
- [59] Nikfetrat K. et al. Prediction of drag at subsonic and transonic speeds using euler methods. aiaa 92-0169. In *30th Aerospace Sciences Meeting and Exhibit*., 1 1992. doi: <https://doi.org/10.2514/6.1992-169>.
- [60] van Dam C. P. Recent experience with different methods of drag prediction. *Progress in Aerospace Sciences*, 35(8):751–798, 11 1999. doi: [https://doi.org/10.1016/S0376-0421\(99\)00009-3](https://doi.org/10.1016/S0376-0421(99)00009-3).
- [61] Darmofal D. Trefftz plane analysis of induced drag, mit opencourseware, 16-100 lectre 19, 2005.
- [62] Embraer. Embraer commercial aviation, 2022. URL <https://www.embraercommercialaviation.com/commercial-jets/erj145/>.
- [63] Jones J. W. Swansim.org, 2022. URL <http://www.swansim.org>.
- [64] Kallinderis Y. and Kwong S. Viscous grids and assessment of the quality. In *15th AIAA Computational Fluid Dynamics Conference*., 2001. doi: <https://doi.org/10.2514/6.2001-2539>.
- [65] Evans B. J. Flite3d github repository, 2022. URL <https://github.com/DrBenEvans/FLITE3D>.
- [66] Knight D. D. Numerical simulation of compressible turbulent flows using the reynolds-averaged navier-stokes equations. agard r-819. In *Turbulence in Compressible Flows. Chapter 5*, 1997. ISBN 92-836-1057-1.
- [67] Sellars N. D. and Hall I. M. An evaluation of advanced cfd codes for stores at incidence. agard cp-570. In *Aerodynamics of Store Integration and Separation. Session 1: Turbulence In Compressible Flows.*, 1995. ISBN 92-836-0022-3.
- [68] Araya G. Turbulence model assessment in compressible flows around complex geometries with unstructured grids. *Fluids*, 4(2):81, 2019. doi: <https://doi.org/10.3390/fluids4020081>.
- [69] Spalart P. R. and Allmaras S. R. A one-equation turbulent model for aerodynamic flows. aiaa paper 92-0439. In *30th Aerospace Sciences Meeting and Exhibit*, 1 1992. doi: <https://doi.org/10.2514/6.1992-439>.

- [70] Mavriplis D. J. and Venkatakrisnan V. A 3d agglomeration multigrid solver for the reynolds-averaged navier-stokes equations on unstructured meshes. *International Journal for Numerical Methods in Fluids*, 23(6): 527–544, 1996. doi: [https://doi.org/10.1002/\(SICI\)1097-0363\(19960930\)23:6<527::AID-FLD429>3.0.CO;2-Z](https://doi.org/10.1002/(SICI)1097-0363(19960930)23:6<527::AID-FLD429>3.0.CO;2-Z).
- [71] Hassan O., Morgan K., and Weatherill N. P. *FLITE SYSTEM Version 4 Theoretical Manual*. Swansea University, 2008.
- [72] Hassan O., Morgan K., and Weatherill N. P. *FLITE SYSTEM Version 4 User Manual*. Swansea University, 2008.
- [73] Chao D. D. and van Dam C. P. Airfoil drag prediction and decomposition. *Journal of aircraft*, 36(4):675–681, 1999. doi: <https://doi.org/10.2514/2.2510>.
- [74] S. C. Smith. Trefftz-plane drag minimization at transonic speeds. *SAE Transactions*, 106:151–161, 1997. URL <http://www.jstor.com/stable/44650390>.
- [75] Monsch S. A study of induced drag and spanwise lift distribution for three-dimensional inviscid flow over a wing. Master’s thesis, Clemson University, 2007.

9 Appendices

9.1 Appendix A

MathWorks MATLAB Function Developed For Trefftz Plane Analysis.

```
function [areaSlice,NDragInduced,CDragInduced] = Trefftz_Custom_Elem(geom,aoastr,plots,filepath,filename,rho,s,V_inf)
%% Trefftz_Custom_Elem
%
% [areaSlice,NDragInduced,CDragInduced] = Trefftz_Custom_Elem(geom,aoastr,plots,filepath,filename,rho,s,V_inf)
%
% INPUT ARGUMENTS
% geom, string, geometry []
% aoastr, string, angle of attack [deg]
% plots, double, 1 = plots
% filepath, char, directory path to trefftz plane data
% filename, char, trefftz plane data filename
% rho, double, density [kg/m^3]
% s, double, wing area [m^2]
% V_inf, double, free stream velocity perpendicular to Trefftz plane [m/s]
%
% OUTPUTS
% areaSlice, double, area of Trefftz plane [m^2]
% NDragInduced, double, Induced Drage [N]
% CDragInduced, double, Coefficient of Induced Drag []
%
% INSTRUCTIONS FOR TREFFTZ PLANE EXTRACTION
% What follows are instructions as how to extract the Trefftz plane
% information used by this function from an EnSight Gold format result
% generated by FLITE3D CFD software, using ANSYS EnSight.
%
% 1) Load your result .case file into ANSYS EnSight.
% 2) Select "External Flowfield 1".
% 3) Create "clip plane" downstream of body in freestream within EnSight
% using selected parts.
% 4) Select ONLY the clip plane.
% 5) Click Calculator
% 6) Scroll and select "EleSize".
% 7) Click "Evaluate for selected parts".
% 08) Click "EleMetric" and select "centroid" in the drop down next to
% "metric_function".
% 09) Click "Evaluate for selected parts".
% 10) Click "NodeToElem" and select "velocity" in the drop down next to
% "nodal scalar or vector".
% 11) Click "Evaluate for selected parts".
% 12) Select in the Variables list
% a) EleMetric
% b) EleSize
% c) NodeToElem
% 13) Click File > Export > Geometric Entities
% 14) Select "Flatfile"
% 15) Enter "EleSize, EleMetric, NodeToElem" into the "Parameter(s)" field.
% 16) Ensure "Save as Binary file(s)" is unticked.
% 17) Export using filename and location of your choice.
% 18) Set "filepath" and "filename" inputs appropriately within this script.
% * note: filename may be appended with "000" from the input filename.
% for example, exporting from ANSYS EnSight in step 17 as "test"
% may actually export "test000".
% 19) Give other inputs appropriate values.
% 20) Call function.

%% Derived

aoa = str2double(aoastr);
filepathname = [filepath, filename];

%% Set up the Import Options and import the data

opts = delimitedTextImportOptions("NumVariables", 7);

% Specify range and delimiter
opts.DataLines = [4, Inf];
opts.Delimiter = ",";

% Specify column names and types
opts.VariableNames = ...
["CellSize", "Centroidx", "Centroidy", "Centroidz", "VelocityElemx", "VelocityElemy", "VelocityElemz", "PresElem"];
opts.VariableTypes = ...
["double", "double", "double", "double", "double", "double", "double"];

% Specify file level properties
opts.ExtraColumnsRule = "ignore";
opts.EmptyLineRule = "read";

% Import the data
tbl = readtable(filepathname, opts);

%% Convert to output type

A = tbl.CellSize; % area of plane / element intersections [m^2]
centroidY = tbl.Centroidy; % centroid y coordinate
centroidZ = tbl.Centroidz; % centroid z coordinate
velocityX = tbl.VelocityElemx; % x velocity
velocityY = tbl.VelocityElemy; % y velocity
```

```

velocityZ = tbl.VelocityElemz;      % z velocity

%% rotate axis & prepare vectors

zfromv = sind(aoa)*V_inf;
xfromv = cosd(aoa)*V_inf;

wfromz = cosd(aoa)*(velocityZ-zfromv);
wfromx = sind(aoa)*(velocityX-xfromv);

z = wfromz - wfromx;

ufromz = sind(aoa)*(velocityZ);
ufromx = cosd(aoa)*(velocityX);

u = ufromz + ufromx;

%% Clear temporary variables

clear opts tbl

%% Calculation

areaSlice = sum(A);

V = velocityY; % vertical velocity perturbations [m/s]
W = z;         % lateral velocity perturbations [m/s]
U = u - V_inf; %freestream velocity perturbations [m/s]

%Integration of wake for Drag-induced force calculation
Drag_induced = (rho/2)*((V.^2)+(W.^2)-(U.^2)).*A; % [N]

%Sum over surface
NDragInduced = sum(Drag_induced);

%Output of Induced Drag Coefficient
CDragInduced = 2*NDragInduced/(rho*V_inf^2*s);

%% Outputs to console

if plots == 1

    fprintf('--- Trefftz Plane Analysis ---\n')
    fprintf('Slice Area = %f [m^2]\n', sum(A))
    fprintf('Input file = %s\n', filepathname)
    fprintf('Wing Area (s) [m^2] = %f\n', s)
    fprintf('Free Stream Velocity (V_inf) [m/s] = %f\n', V_inf)
    fprintf('Free Stream Density (rho) [kg/m^3] = %f\n', rho)
    fprintf('Induced Drag Force (D_i) [N] = %f\n', NDragInduced)
    fprintf('Coefficient of Induced Drag (C_D_i) [] = %f\n\n', CDragInduced)

    clear filepathname

    % create and format figure
    figure
    hold on
    daspect([1 1 1])
    title_string = sprintf('Velocity on Trefftz Plane | %s | AoA = %.0f deg',geom,aoa);
    title(title_string)
    subtitle_string = ...
        sprintf('Induced Drag Force (D_i) = %.1f N\Coefficient of Induced Drag (CD_i) = %.3f',NDragInduced,CDragInduced);
    subtitle(subtitle_string)
    xlabel('y, m')
    ylabel('z, m')
    axis([-150 0 -150 150])

    % plot vector arrows
    q = quiver(centroidY,centroidZ,V,W);
    mags = sqrt(sum(cat(2, q.UData(:), q.VData(:), reshape(q.WData, numel(q.UData), []).^2, 2)));
    currentColormap = colormap(gca);
    [~,~,ind] = histcounts(mags, size(currentColormap, 1));
    cmap = uint8(ind2rgb(ind(:), currentColormap) * 255);
    cmap(:,4) = 255;
    cmap = permute( repmat(cmap, [1 3 1]), [2 1 3]);
    set(q.Head, 'ColorBinding', 'interpolated', 'ColorData', reshape(cmap(1:3,:,:), [], 4).');
    set(q.Tail, 'ColorBinding', 'interpolated', 'ColorData', reshape(cmap(1:2,:,:), [], 4).');
    c = colorbar;

    labelstring = sprintf('nonxvel / nonxvel_m_a_x (%.2f ms^-1)',max(sqrt((velocityY.^2)+(velocityZ.^2))));

    c.Label.String = labelstring;

    % additional plots
    viscircles([0,0],1.14,'Color','k','LineWidth',2.0);
    plot([0,-10.02],[-1.14,-0.49],'k','LineWidth',2.0)

    if (strcmp(geom,'DW')) || (strcmp(geom,'CW'))
        plot([-10.02,-10.40],[-0.49,-0.05],'k','LineWidth',2.0)
    end

    fig = gcf;

    saveas((figure(fig.Number)), fullfile(sprintf('%s%s',filepath,geom,aoastr)), 'fig')
    saveas((figure(fig.Number)), fullfile(sprintf('%s%s',filepath,geom,aoastr)), 'png')

end
end

```


9.2 Appendix B

Far-Field Trefftz plane slices output by the function presented in appendix A, section 9.1.

Velocity on Trefftz Plane | CW | AoA = 0 deg

Induced Drag Force (D_i) = 1249.2 N

Coefficient of Induced Drag (CD_i) = 0.004

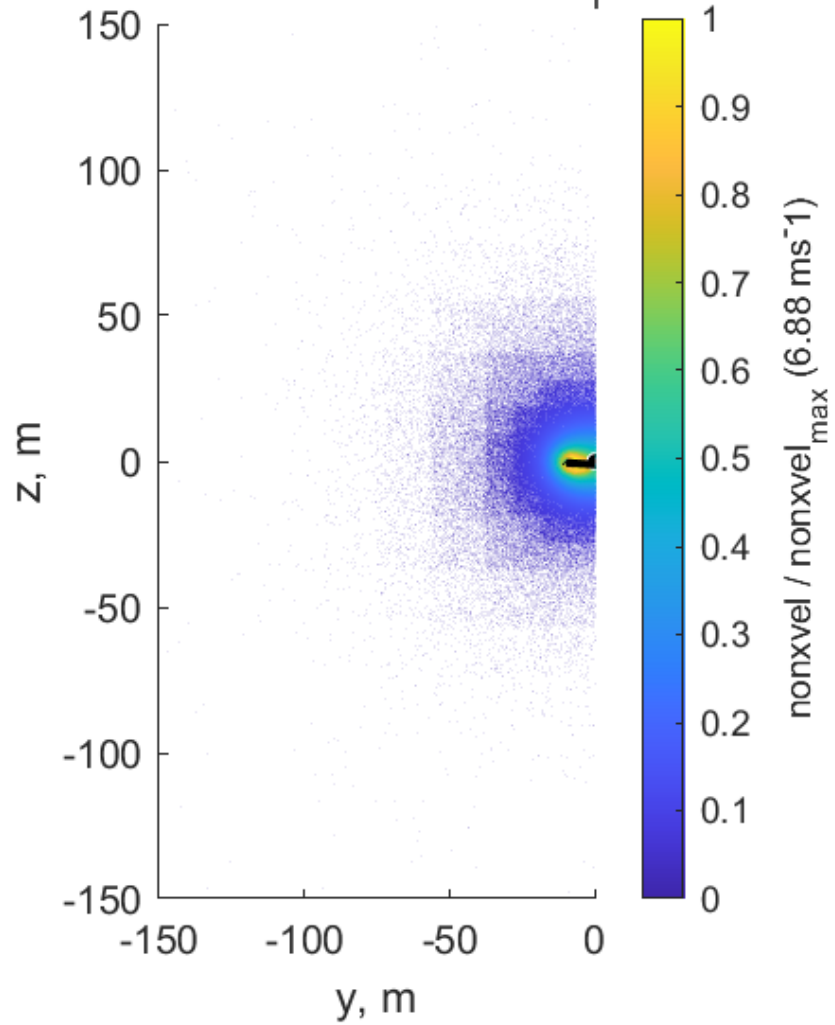


Figure 26: Trefftz Plane Analysis Of CW At Angle Of Attack = 0 Deg

Velocity on Trefftz Plane | CW | AoA = 1 deg

Induced Drag Force (D_i) = 2339.5 N

Coefficient of Induced Drag (CD_i) = 0.007

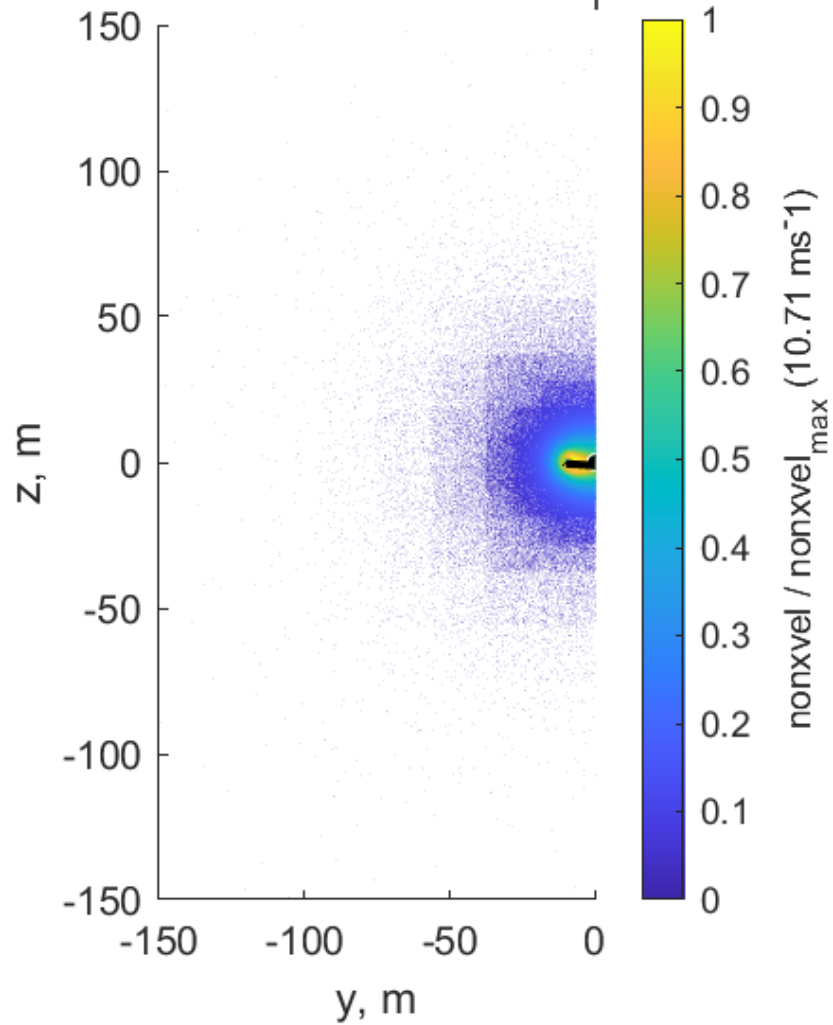


Figure 27: Trefftz Plane Analysis Of CW At Angle Of Attack = 1 Deg

Velocity on Trefftz Plane | CW | AoA = 2 deg

Induced Drag Force (D_i) = 3461.6 N

Coefficient of Induced Drag (CD_i) = 0.011

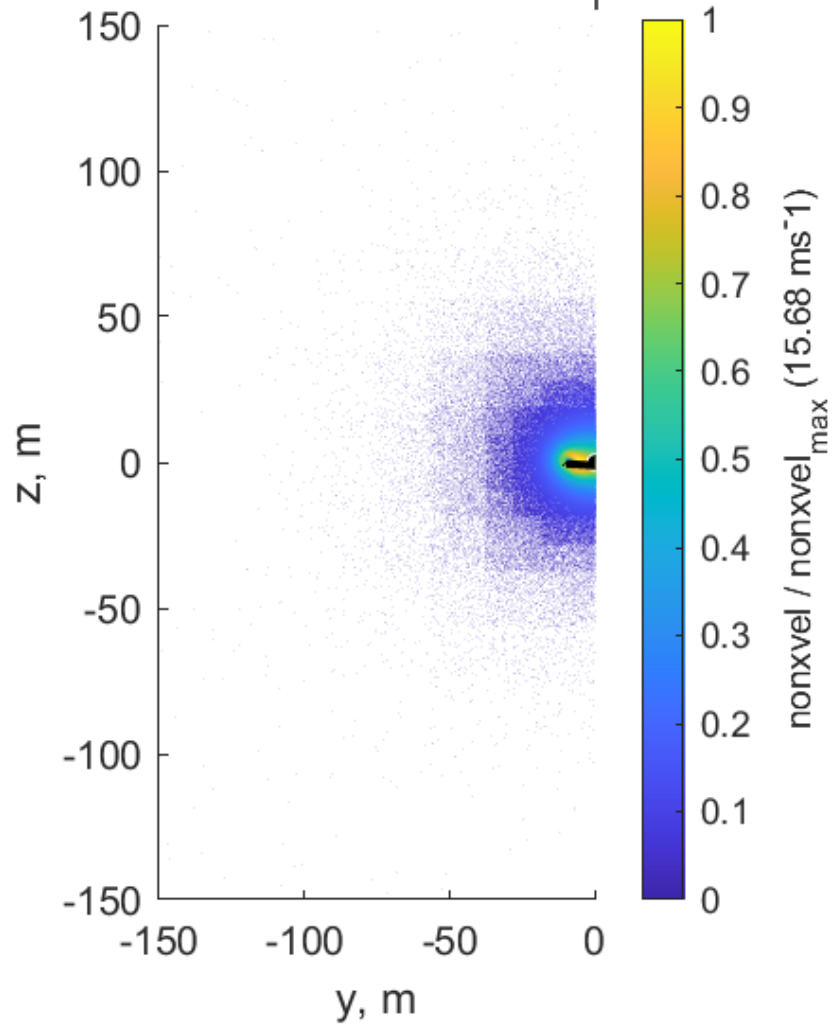


Figure 28: Trefftz Plane Analysis Of CW At Angle Of Attack = 2 Deg

Velocity on Trefftz Plane | CW | AoA = 3 deg

Induced Drag Force (D_i) = 4692.5 N

Coefficient of Induced Drag (CD_i) = 0.015

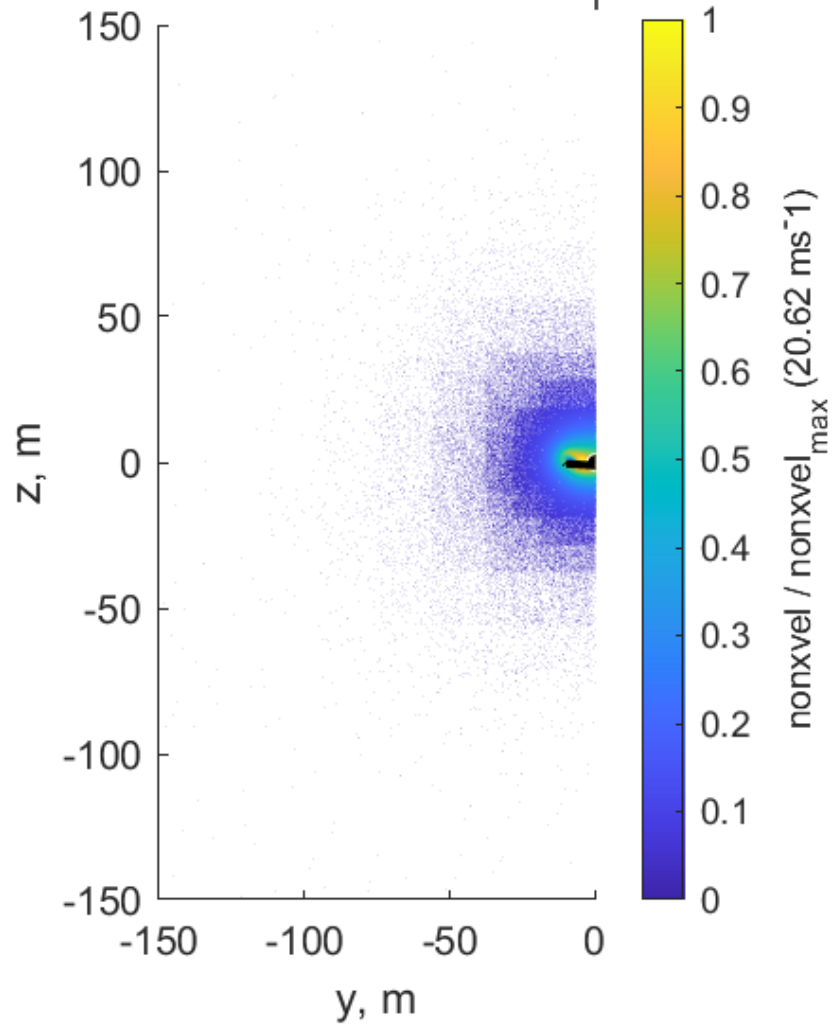


Figure 29: Trefftz Plane Analysis Of CW At Angle Of Attack = 3 Deg

Velocity on Trefftz Plane | CW | AoA = 4 deg

Induced Drag Force (D_i) = 5769.1 N

Coefficient of Induced Drag (CD_i) = 0.018

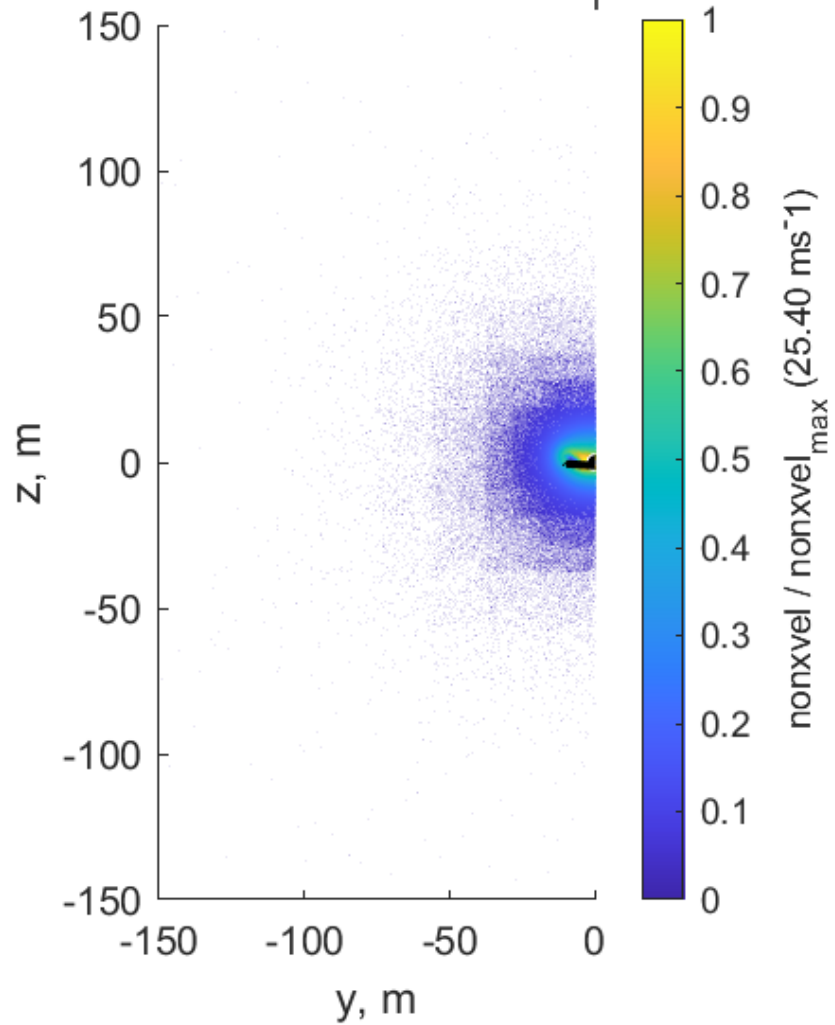


Figure 30: Trefftz Plane Analysis Of CW At Angle Of Attack = 4 Deg

Velocity on Trefftz Plane | CW | AoA = 5 deg

Induced Drag Force (D_i) = 6715.7 N

Coefficient of Induced Drag (CD_i) = 0.021

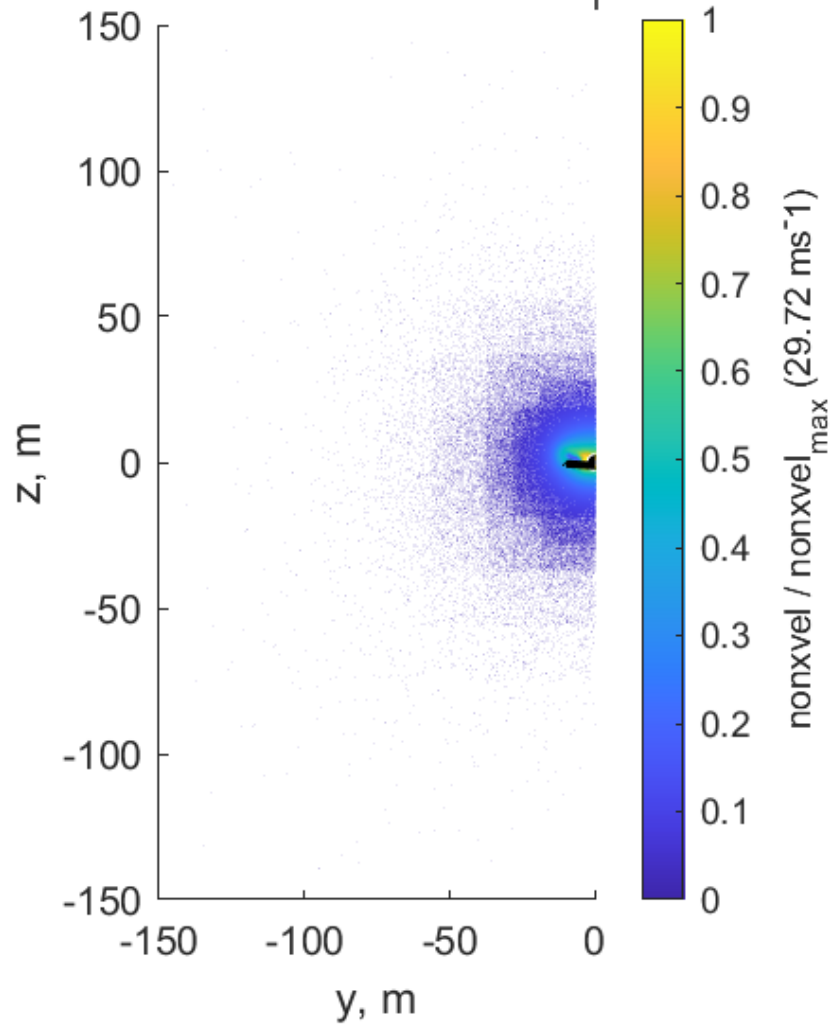


Figure 31: Trefftz Plane Analysis Of CW At Angle Of Attack = 5 Deg

Velocity on Trefftz Plane | DW | AoA = 0 deg

Induced Drag Force (D_i) = 1220.9 N

Coefficient of Induced Drag (CD_i) = 0.004

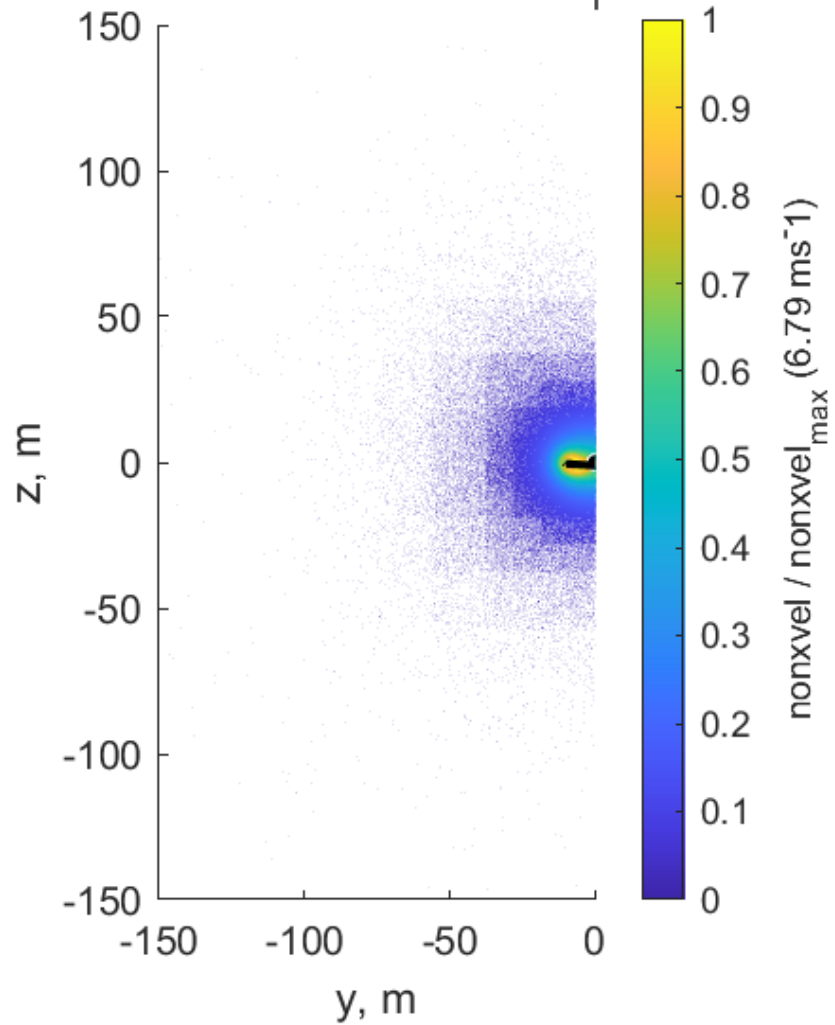


Figure 32: Trefftz Plane Analysis Of DW At Angle Of Attack = 0 Deg

Velocity on Trefftz Plane | DW | AoA = 1 deg

Induced Drag Force (D_i) = 2255.6 N

Coefficient of Induced Drag (CD_i) = 0.007

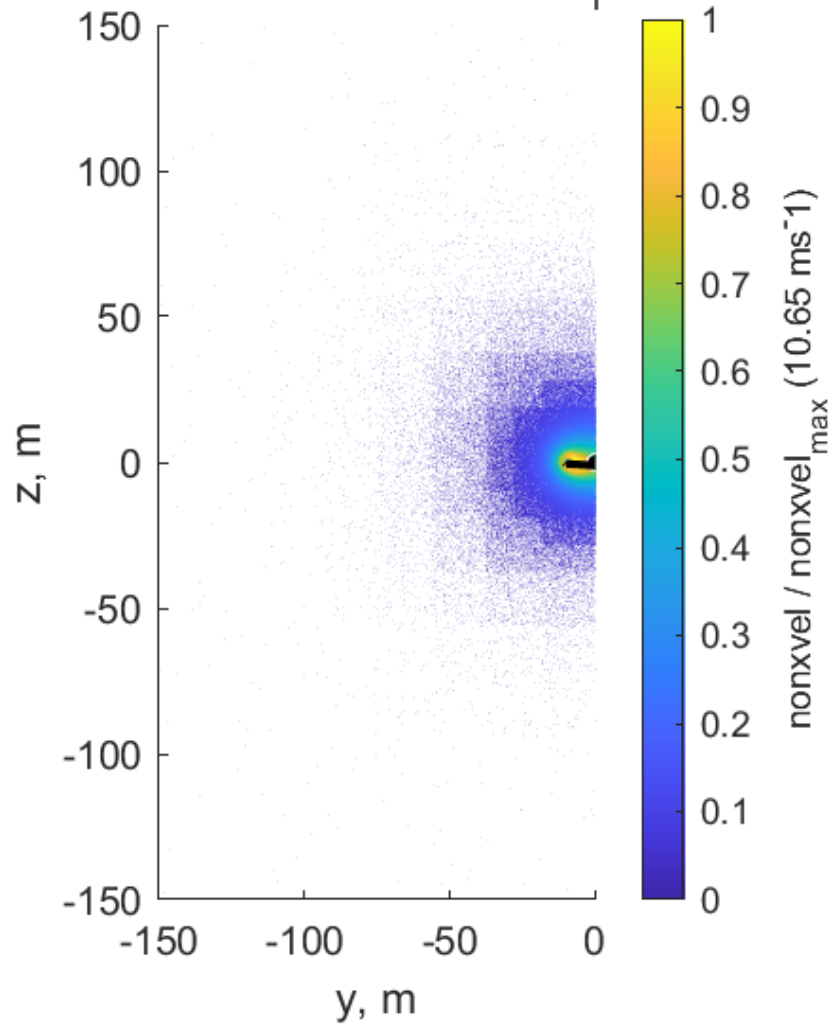


Figure 33: Trefftz Plane Analysis Of DW At Angle Of Attack = 1 Deg

Velocity on Trefftz Plane | DW | AoA = 2 deg

Induced Drag Force (D_i) = 3378.9 N

Coefficient of Induced Drag (CD_i) = 0.011

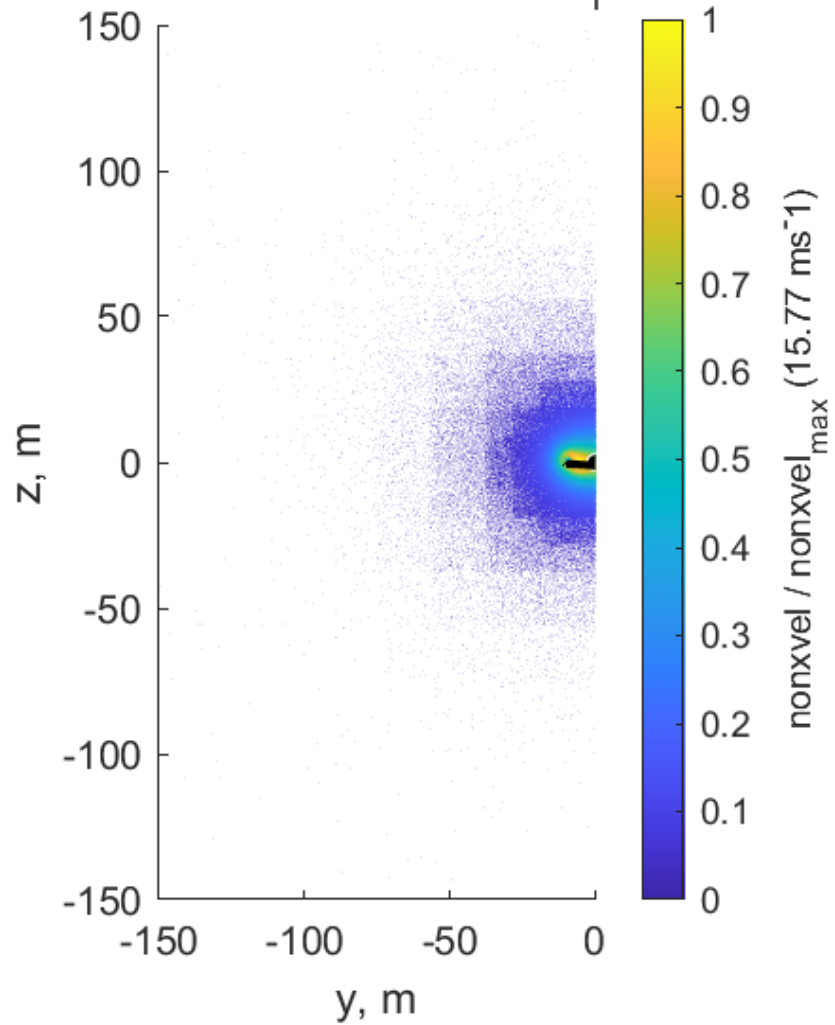


Figure 34: Trefftz Plane Analysis Of DW At Angle Of Attack = 2 Deg

Velocity on Trefftz Plane | DW | AoA = 3 deg

Induced Drag Force (D_i) = 4562.3 N

Coefficient of Induced Drag (CD_i) = 0.014

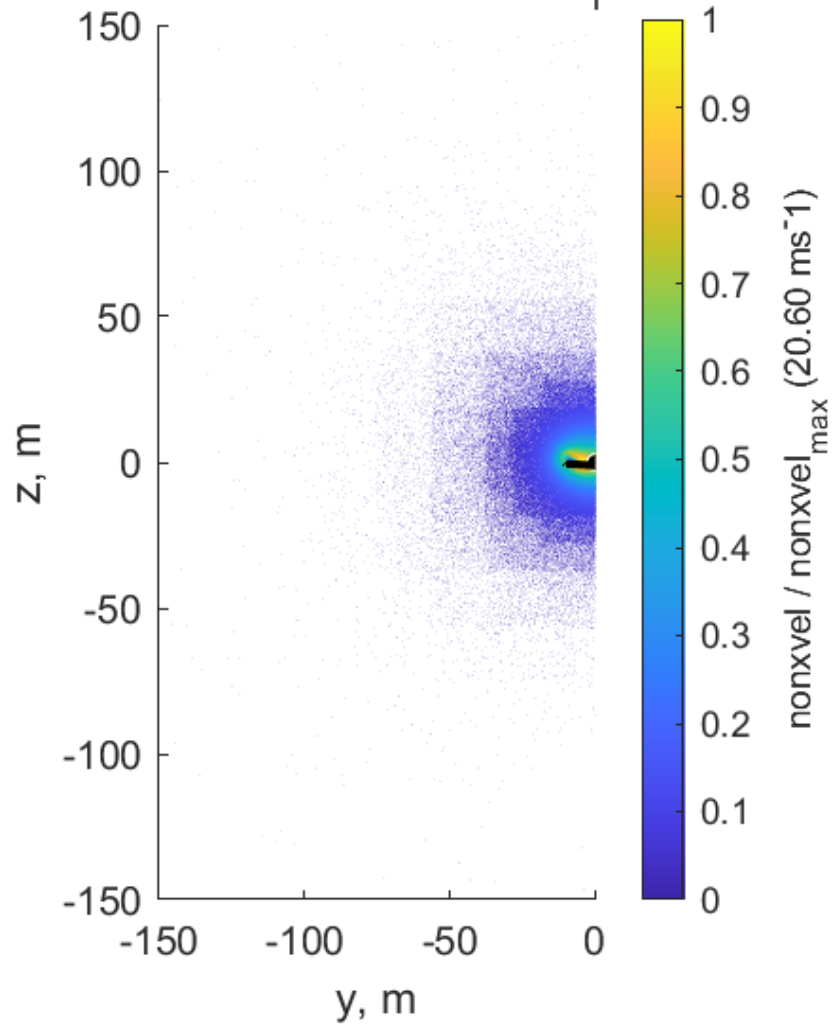


Figure 35: Trefftz Plane Analysis Of DW At Angle Of Attack = 3

Velocity on Trefftz Plane | DW | AoA = 4 deg

Induced Drag Force (D_i) = 5703.4 N

Coefficient of Induced Drag (CD_i) = 0.018

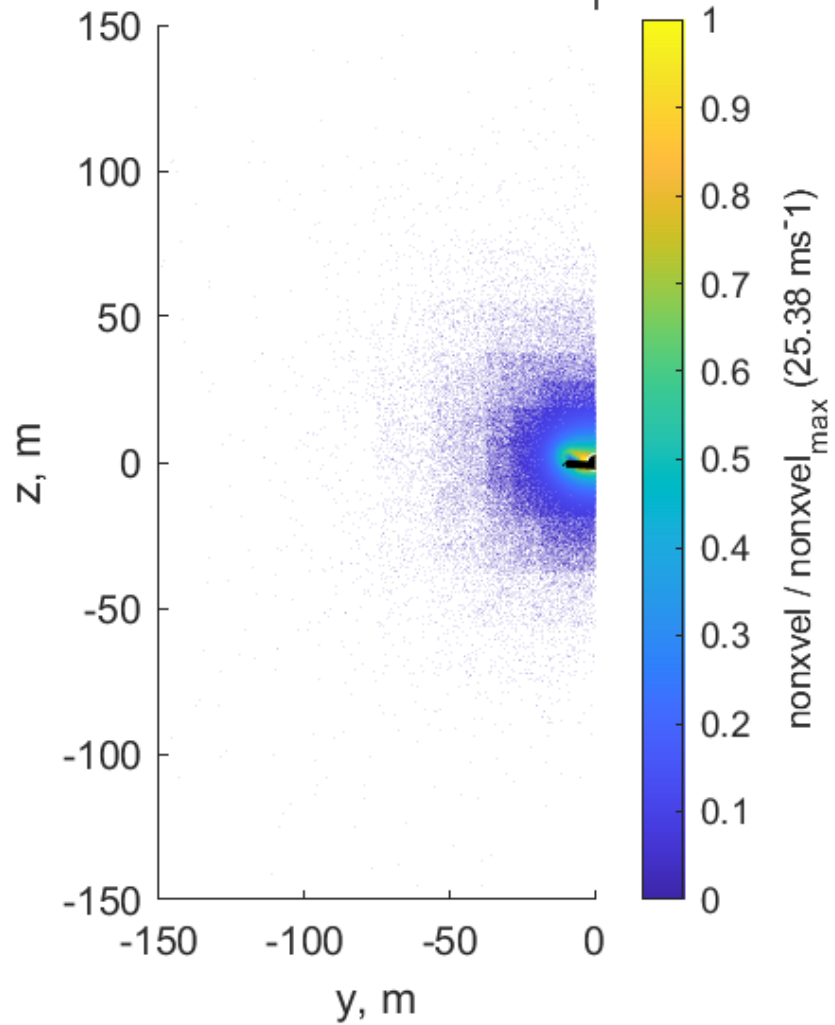


Figure 36: Trefftz Plane Analysis Of DW At Angle Of Attack = 4

Velocity on Trefftz Plane | DW | AoA = 5 deg

Induced Drag Force (D_i) = 6592.9 N

Coefficient of Induced Drag (CD_i) = 0.021

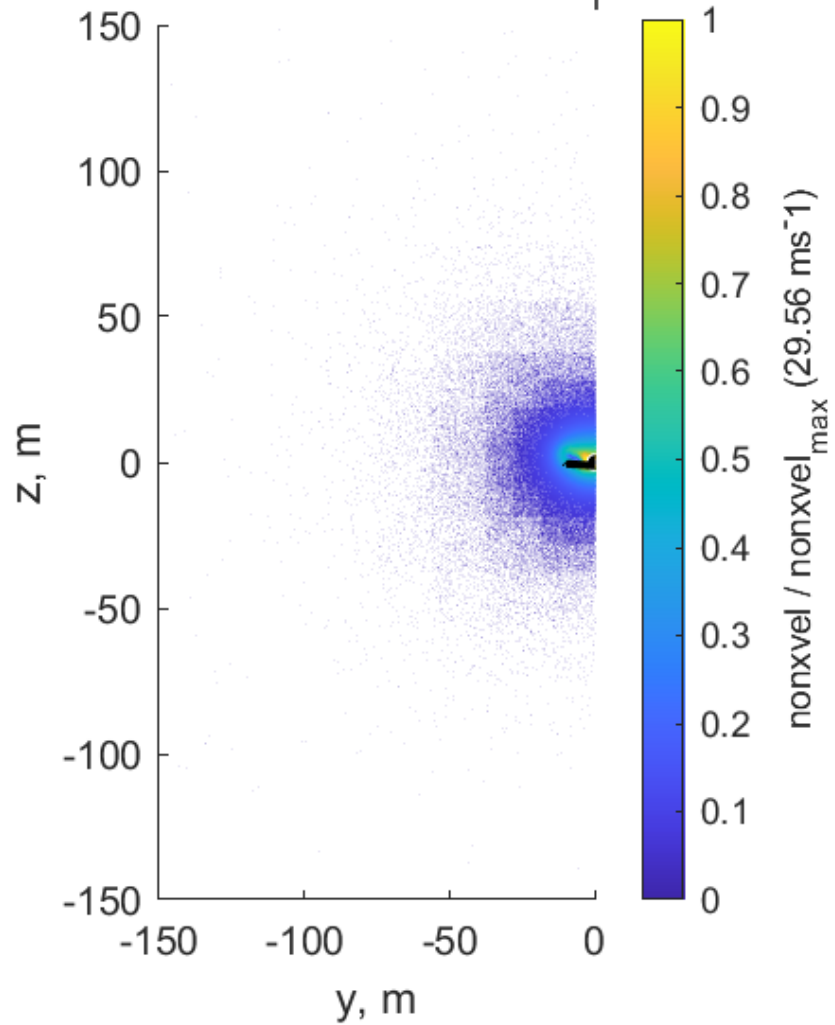


Figure 37: Trefftz Plane Analysis Of DW At Angle Of Attack = 5 Deg

Velocity on Trefftz Plane | ST | AoA = 0 deg

Induced Drag Force (D_i) = 1246.7 N

Coefficient of Induced Drag (CD_i) = 0.004

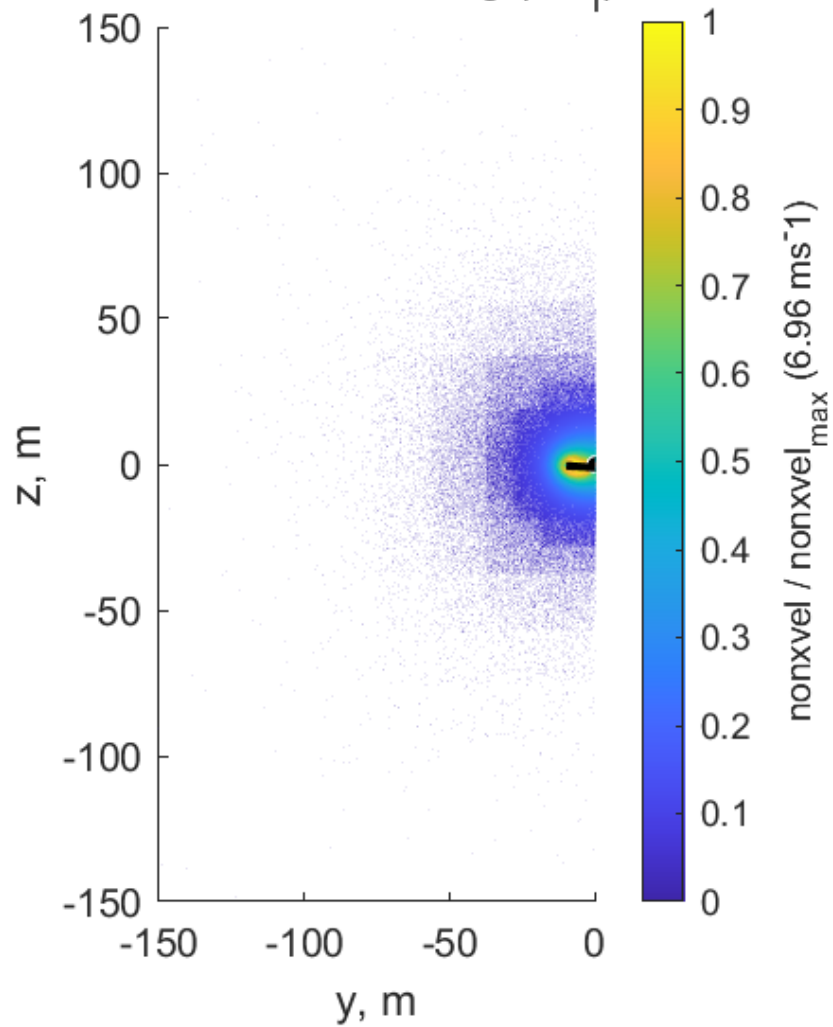


Figure 38: Trefftz Plane Analysis Of ST At Angle Of Attack = 0 Deg

Velocity on Trefftz Plane | ST | AoA = 1 deg

Induced Drag Force (D_i) = 2332.6 N

Coefficient of Induced Drag (CD_i) = 0.007

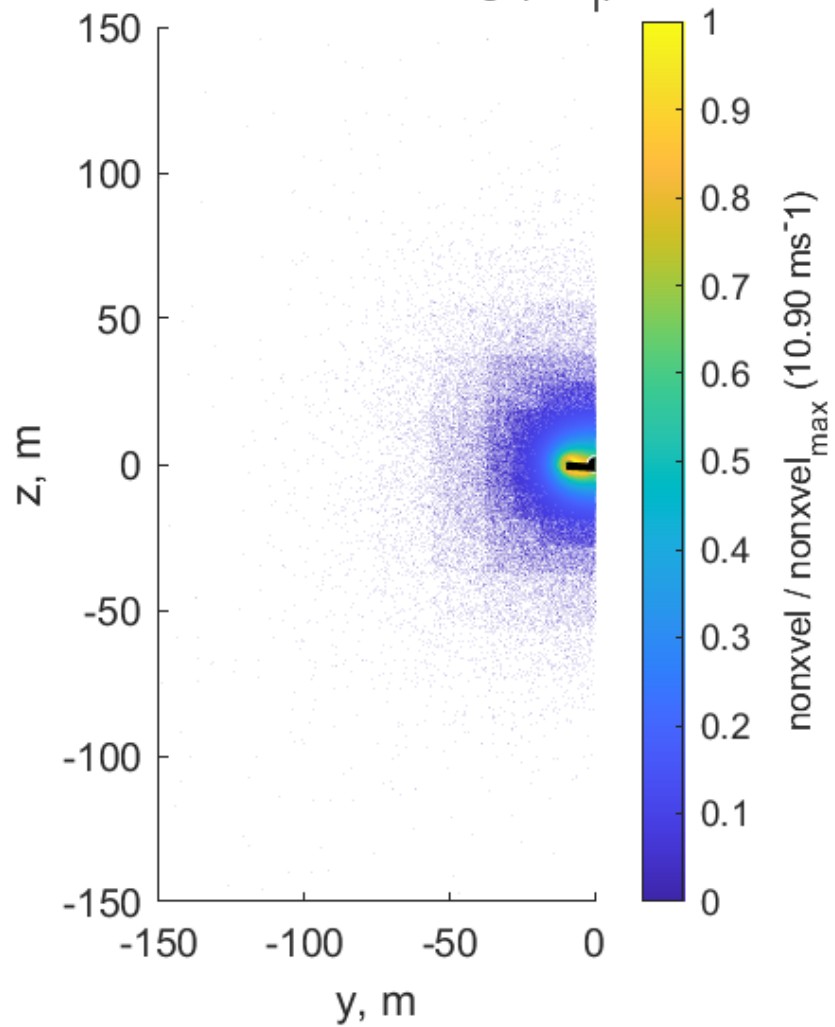


Figure 39: Trefftz Plane Analysis Of ST At Angle Of Attack = 1 Deg

Velocity on Trefftz Plane | ST | AoA = 2 deg

Induced Drag Force (D_i) = 3486.9 N

Coefficient of Induced Drag (CD_i) = 0.011

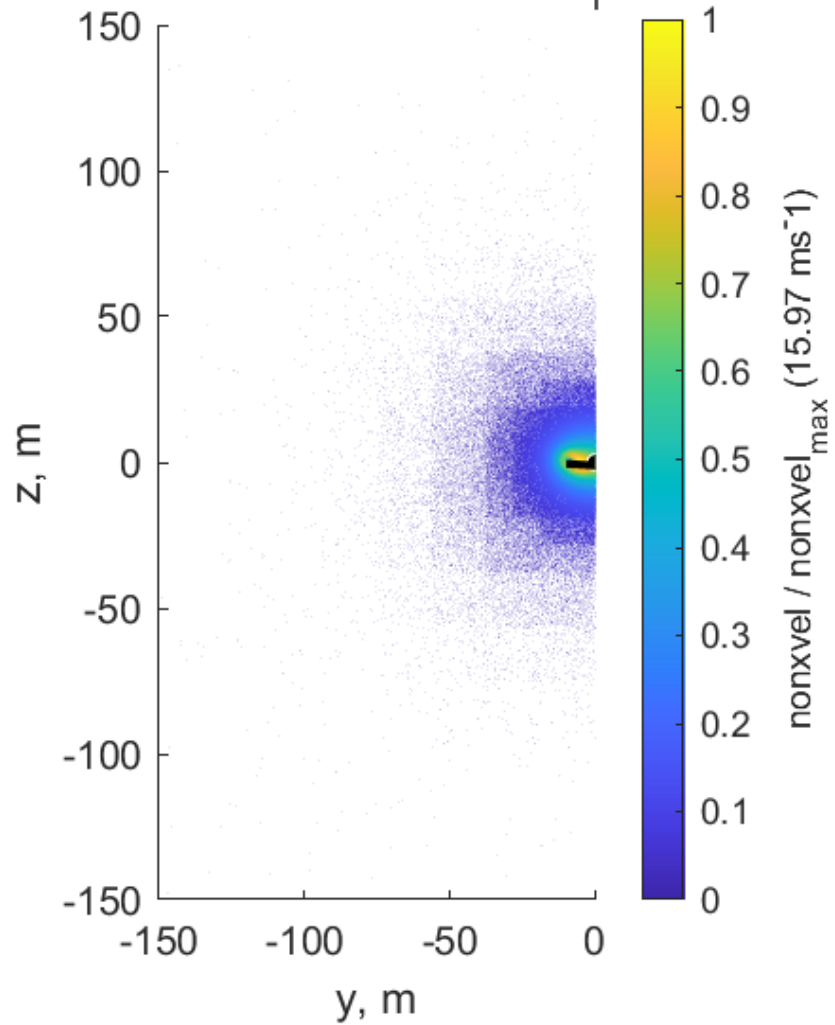


Figure 40: Trefftz Plane Analysis Of ST At Angle Of Attack = 2 Deg

Velocity on Trefftz Plane | ST | AoA = 3 deg

Induced Drag Force (D_i) = 4717.6 N

Coefficient of Induced Drag (CD_i) = 0.015

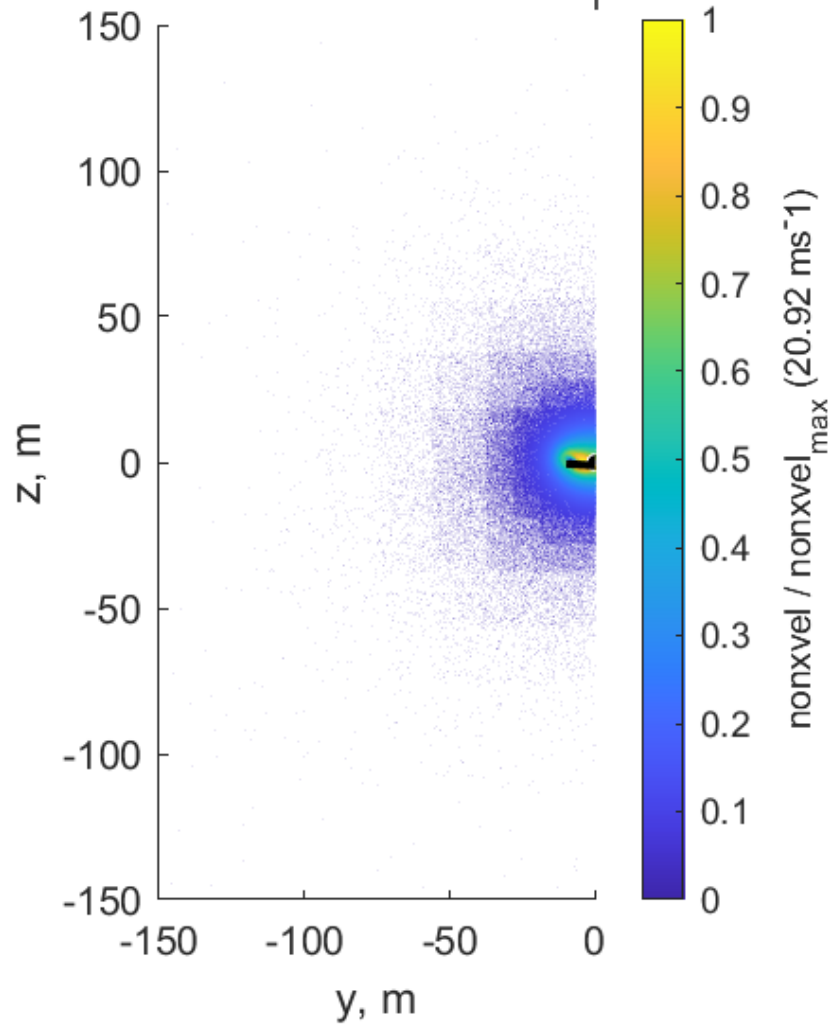


Figure 41: Trefftz Plane Analysis Of ST At Angle Of Attack = 3 Deg

Velocity on Trefftz Plane | ST | AoA = 4 deg

Induced Drag Force (D_i) = 5774.0 N

Coefficient of Induced Drag (CD_i) = 0.018

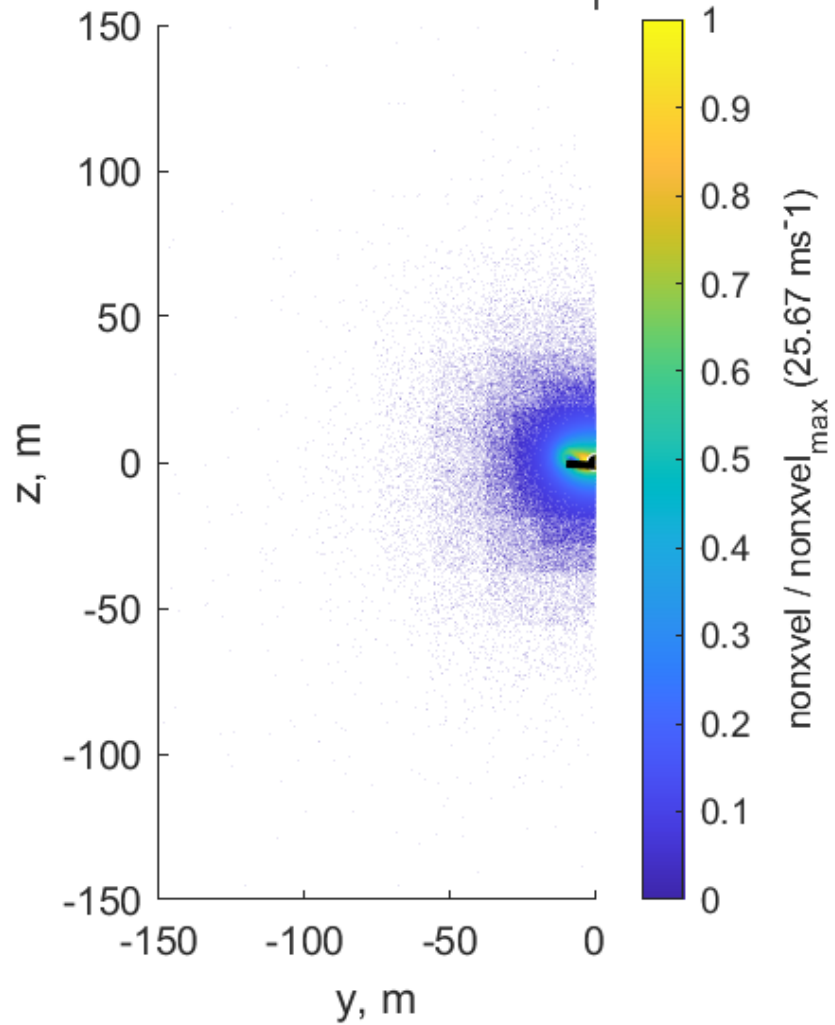


Figure 42: Trefftz Plane Analysis Of ST At Angle Of Attack = 4 Deg

Velocity on Trefftz Plane | ST | AoA = 5 deg

Induced Drag Force (D_i) = 6779.5 N

Coefficient of Induced Drag (CD_i) = 0.022

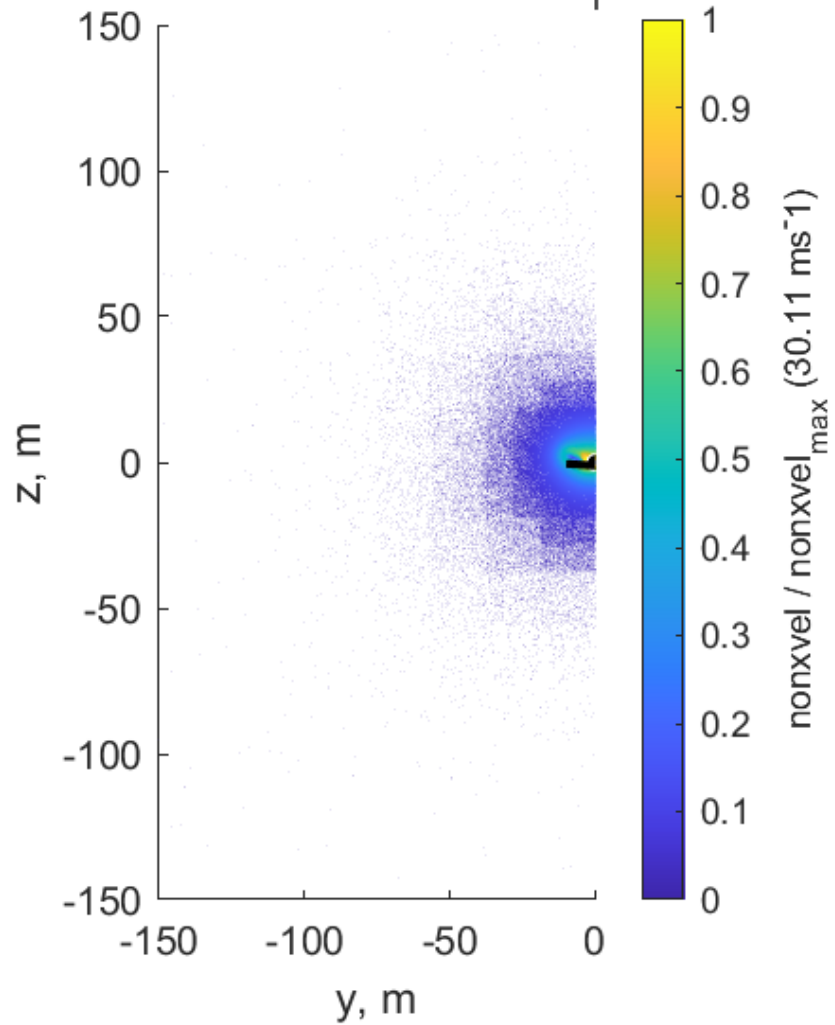


Figure 43: Trefftz Plane Analysis Of ST At Angle Of Attack = 5 Deg

9.3 Appendix C

Path lines showing flow through the ducted winglet (duct highlighted in blue) at each angle of attack.

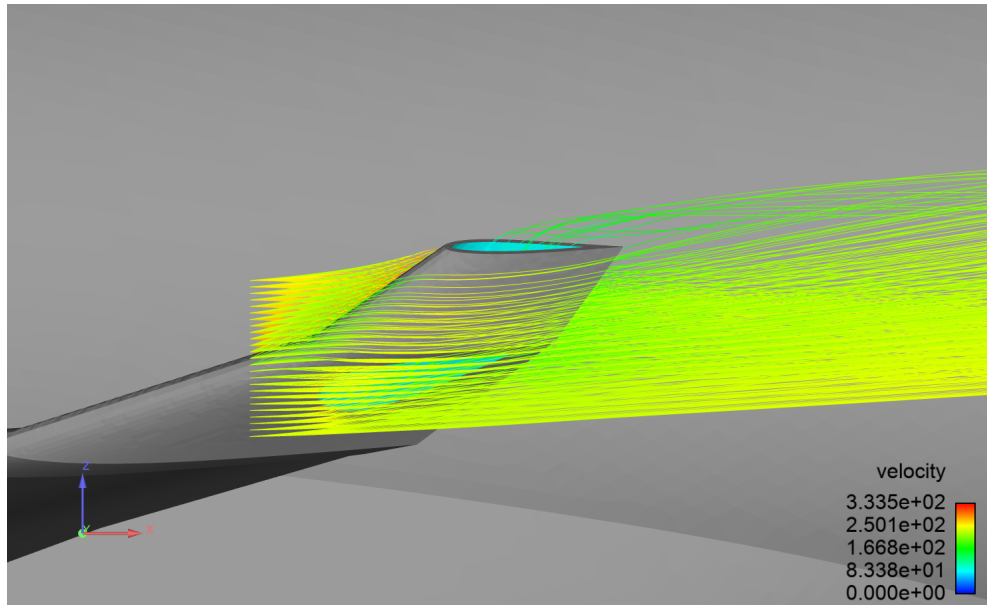


Figure 44: DW Path Lines At Angle Of Attack = 0 Deg

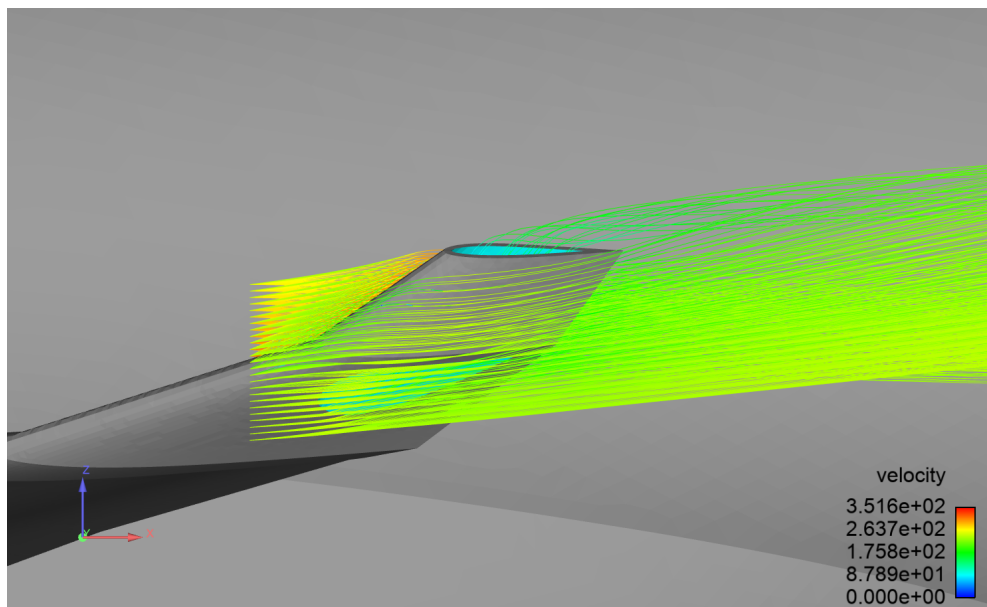


Figure 45: DW Path Lines At Angle Of Attack = 1 Deg

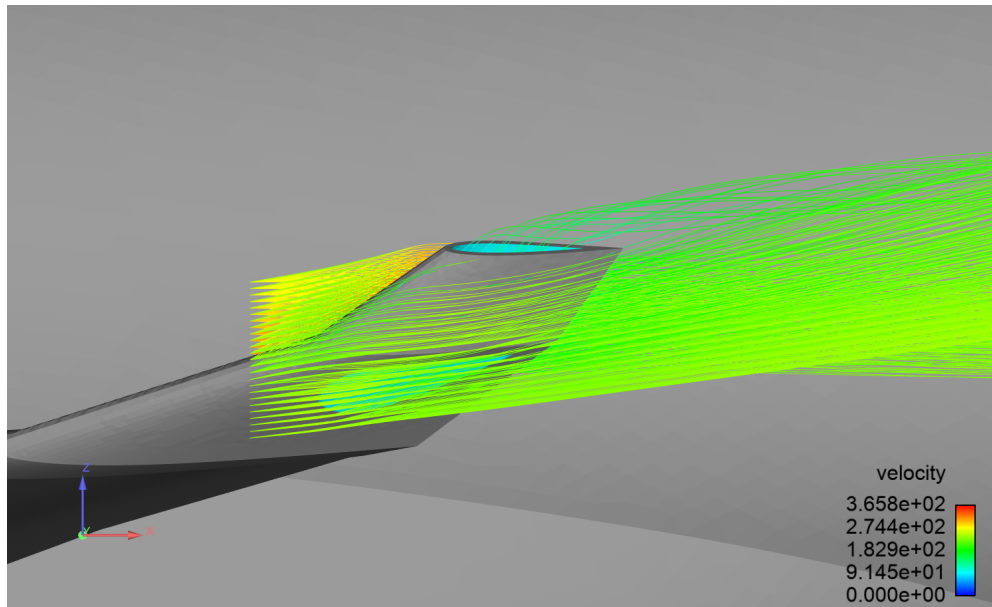


Figure 46: DW Path Lines At Angle Of Attack = 2 Deg

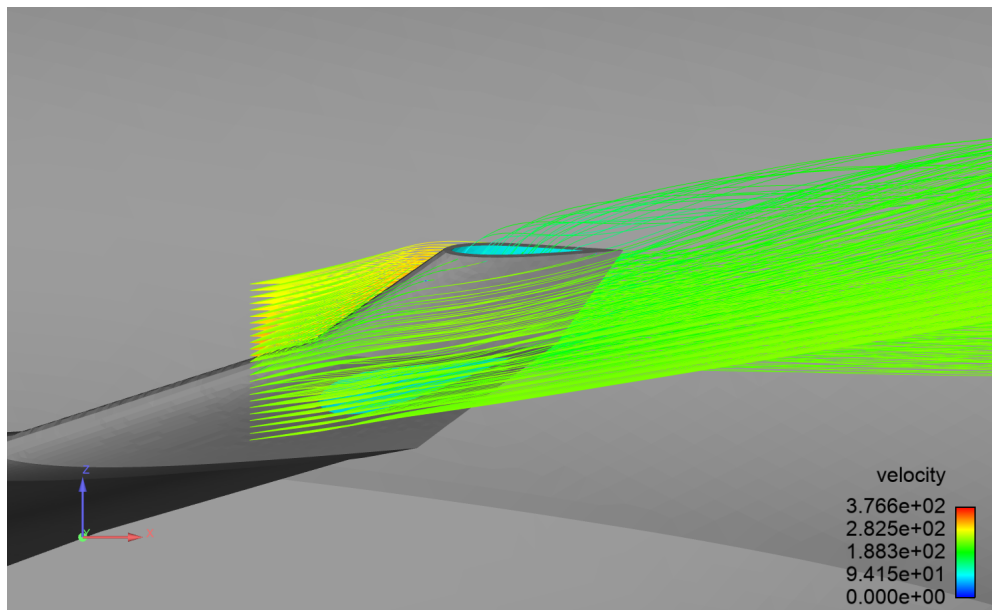


Figure 47: DW Path Lines At Angle Of Attack = 3 Deg

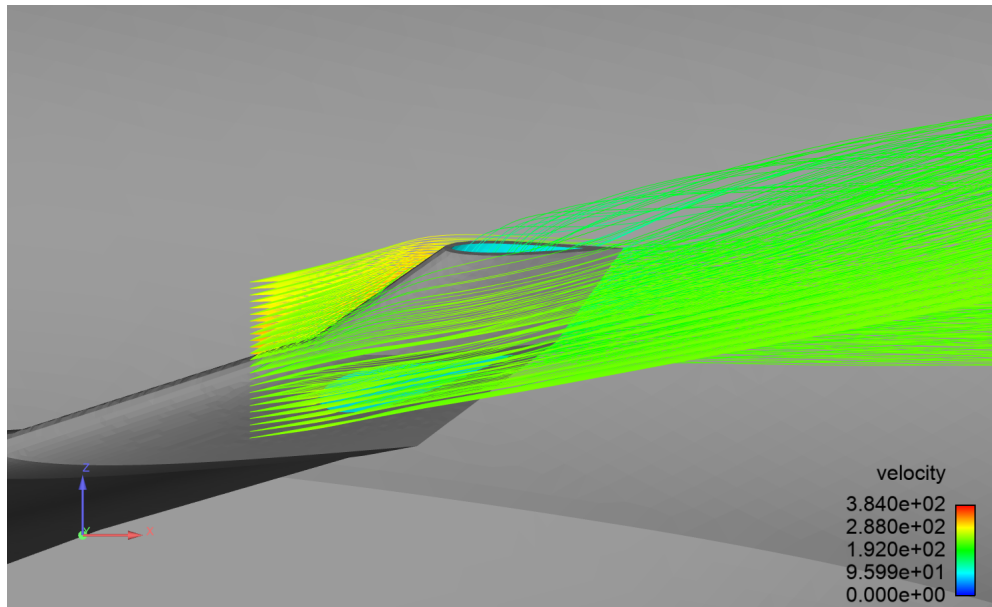


Figure 48: DW Path Lines At Angle Of Attack = 4 Deg

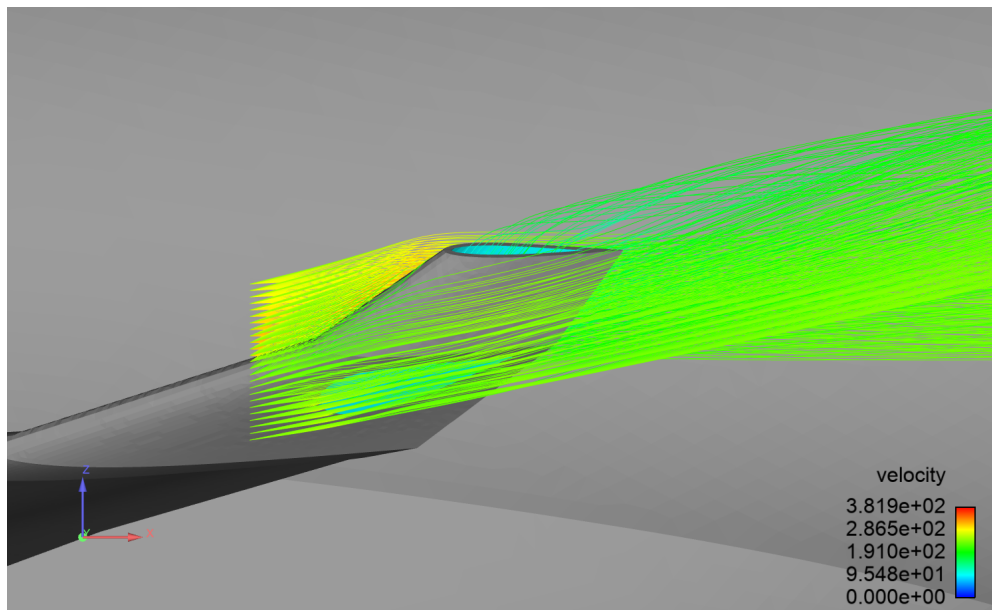


Figure 49: DW Path Lines At Angle Of Attack = 5 Deg

9.4 Appendix D

Velocity on plane through interior of ducted winglet.

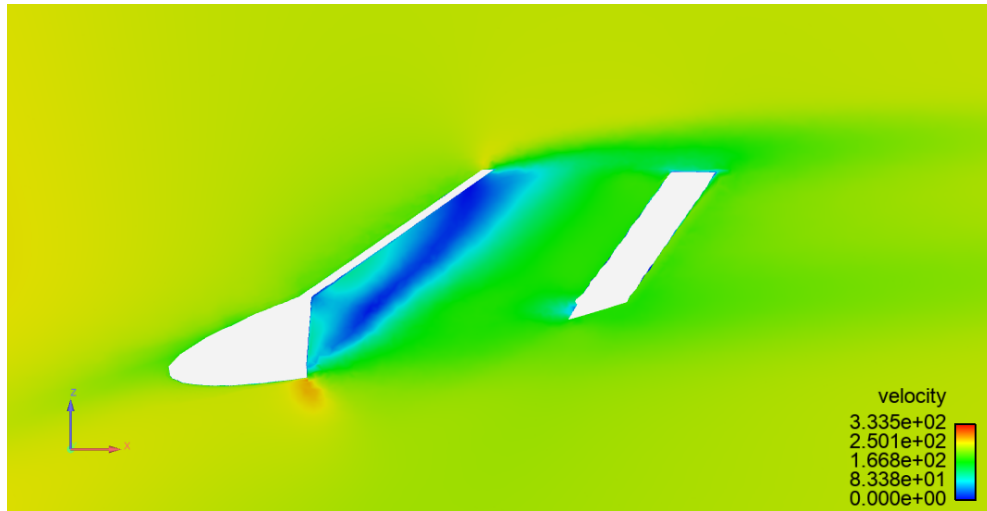


Figure 50: Duct Velocity Plane At Angle Of Attack = 0 Deg

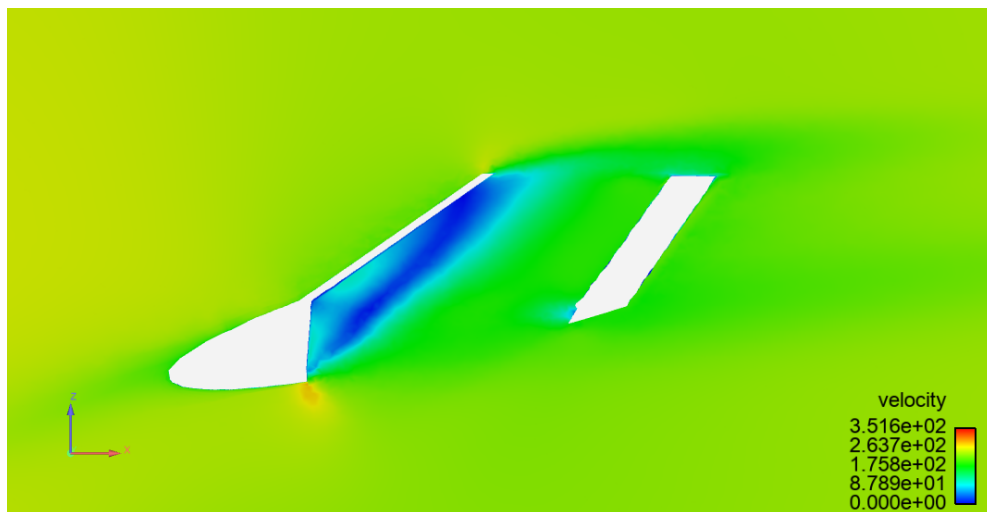


Figure 51: Duct Velocity Plane At Angle Of Attack = 1 Deg

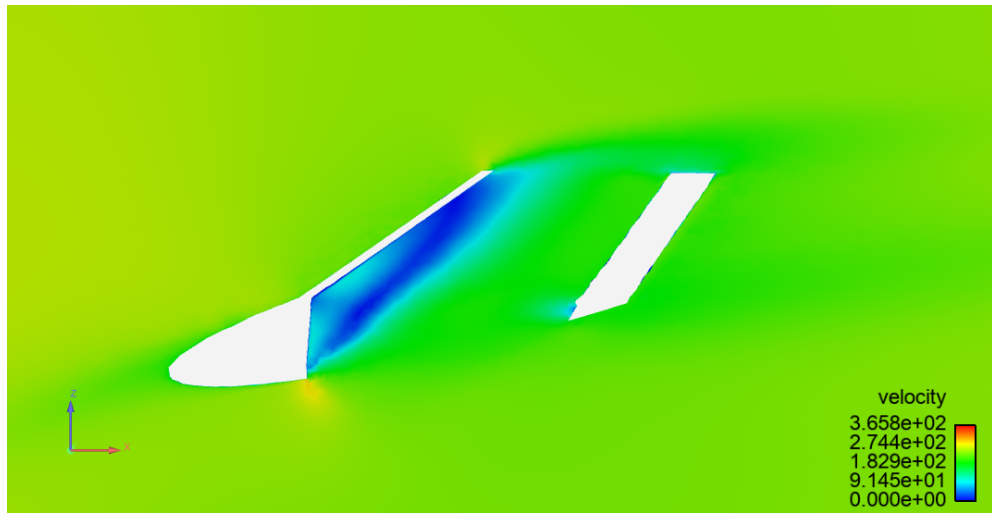


Figure 52: Duct Velocity Plane At Angle Of Attack = 2 Deg

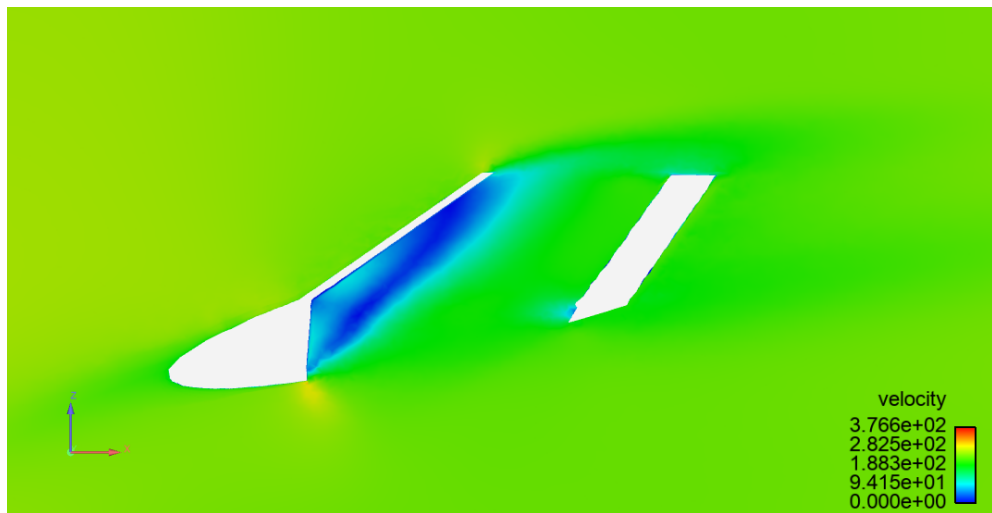


Figure 53: Duct Velocity Plane At Angle Of Attack = 3 Deg

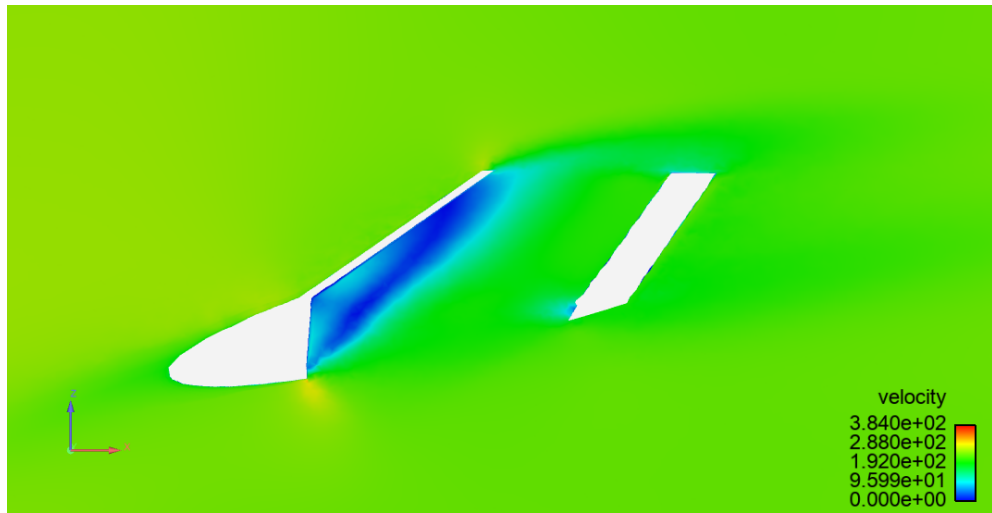


Figure 54: Duct Velocity Plane At Angle Of Attack = 4 Deg

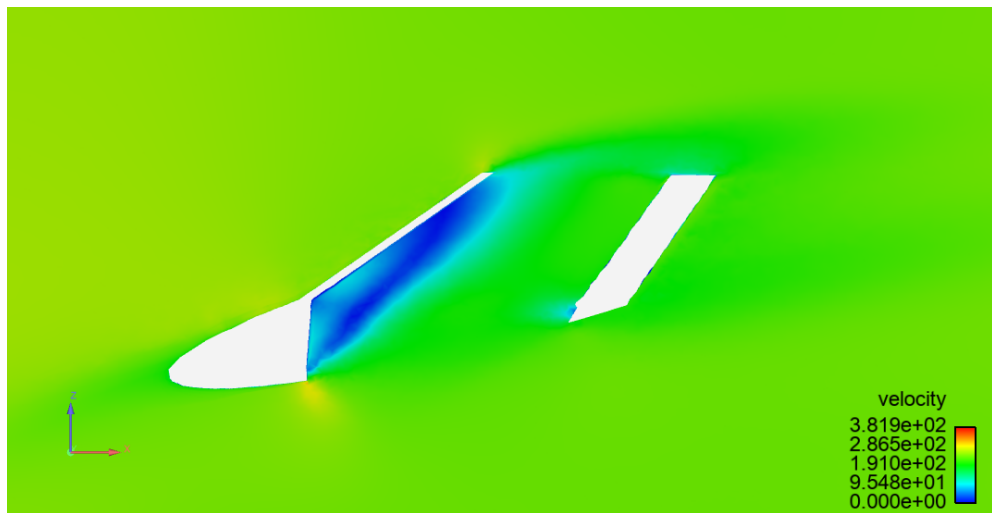


Figure 55: Duct Velocity Plane At Angle Of Attack = 5 Deg

9.5 Appendix E

Velocity vectors on plane through interior of ducted winglet.

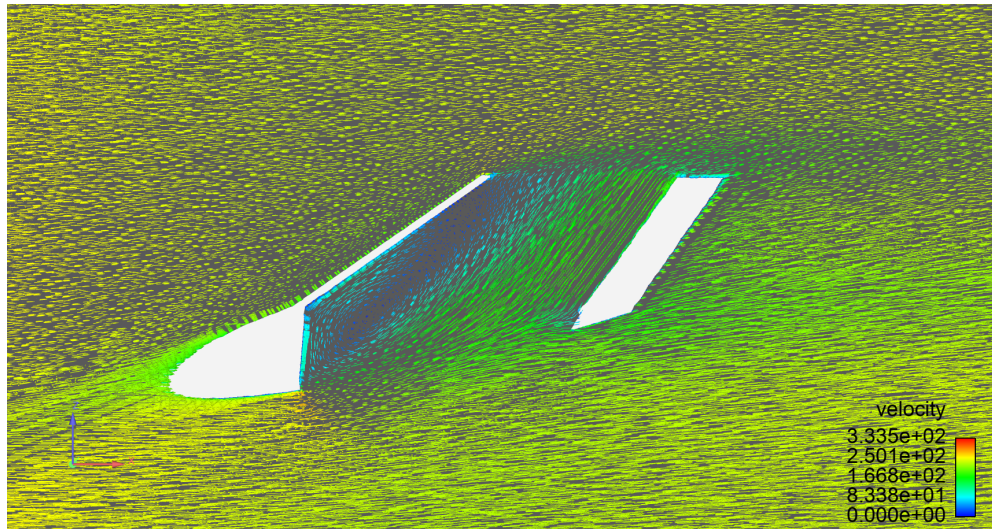


Figure 56: Duct Velocity Plane Vectors At Angle Of Attack = 0 Deg

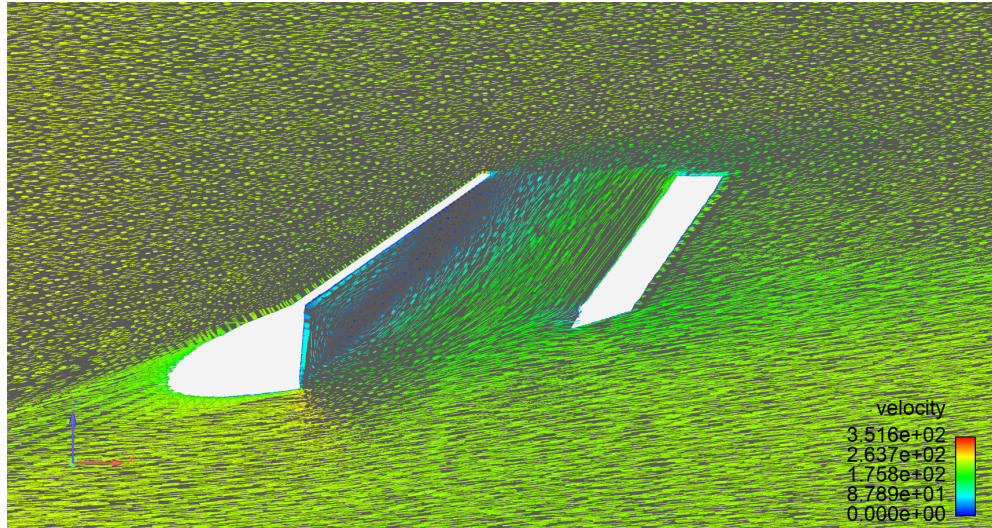


Figure 57: Duct Velocity Plane Vectors At Angle Of Attack = 1 Deg

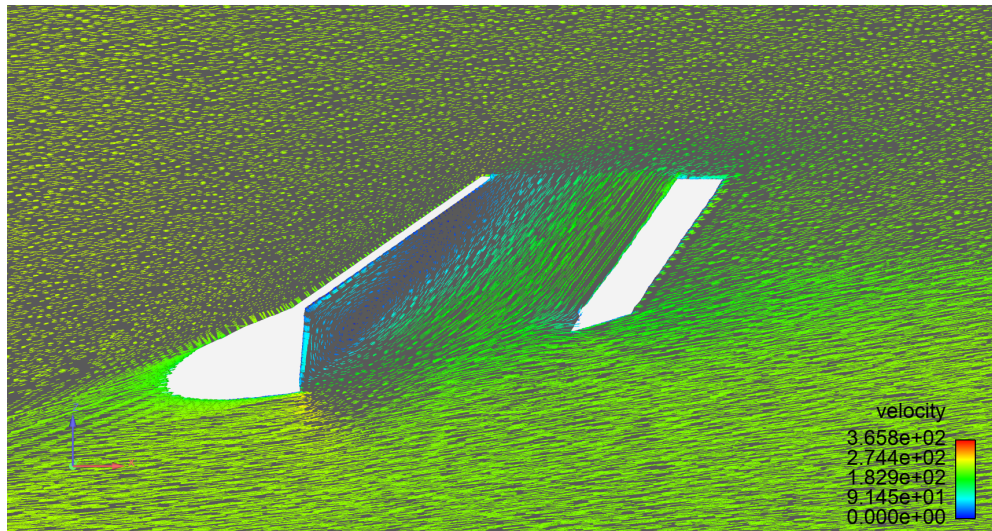


Figure 58: Duct Velocity Plane Vectors At Angle Of Attack = 2 Deg

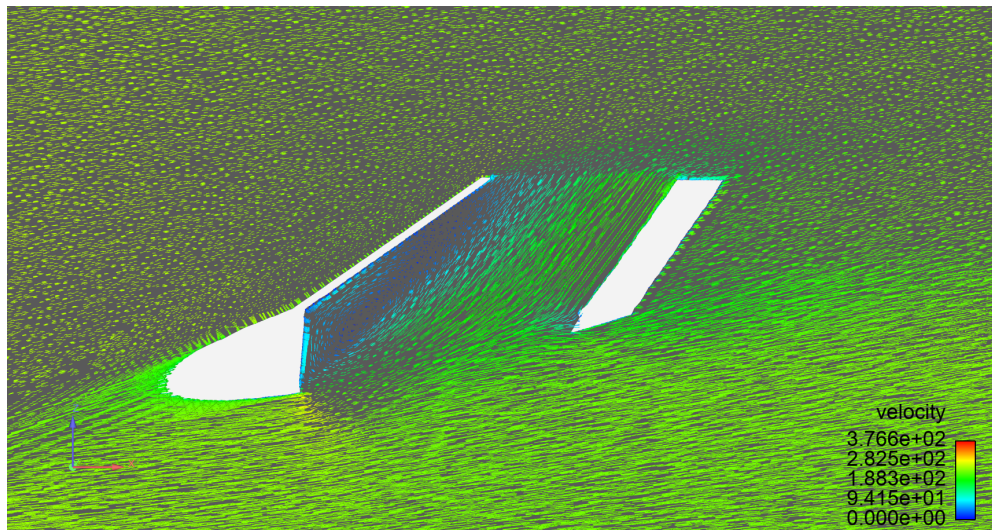


Figure 59: Duct Velocity Plane Vectors At Angle Of Attack = 3 Deg

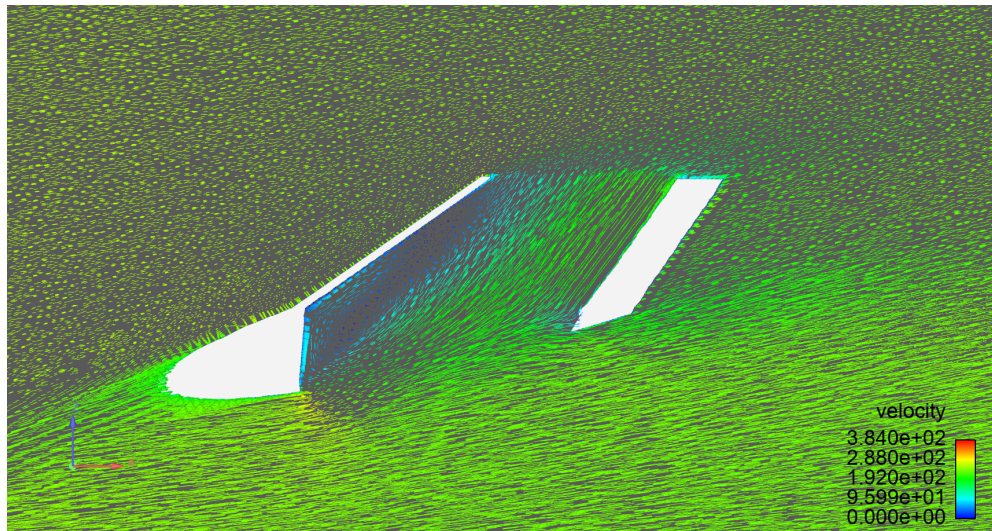


Figure 60: Duct Velocity Plane Vectors At Angle Of Attack = 4 Deg

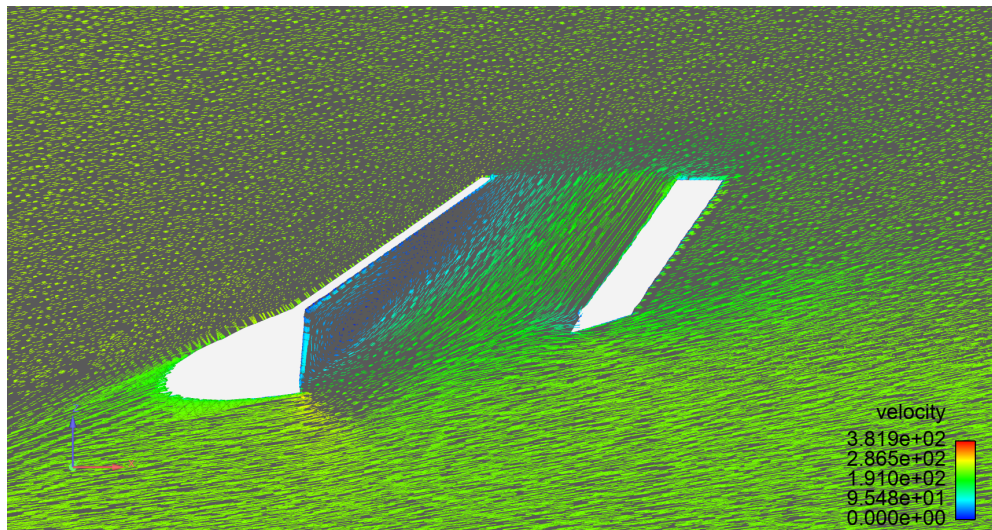


Figure 61: Duct Velocity Plane Vectors At Angle Of Attack = 5 Deg

9.6 Appendix F

Figure showing convergence of the coefficient of drag for all studies.

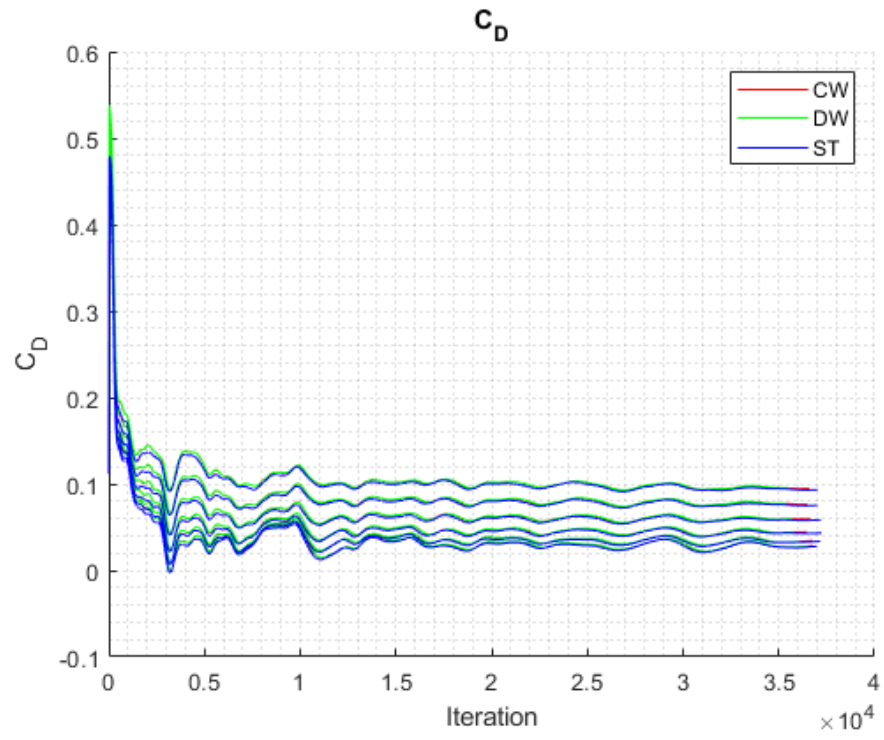


Figure 62: C_D Convergence Of All Studies.